TUDelft

Delft University of Technology

Insights into the structure of the Mongol-Okhotsk suture zone, Adaatsag ophiolite, and tectonic boundaries of the Central Asian Orogenic Belt (Mongolia) from electrical resistivity imaging and seismic velocity models

Comeau, Matthew J.; Rigaud, Rafael; Batmagnai, Erdenechimeg; Tserendug, Shoovdor; Kuvshinov, Alexey; Becken, Michael; Demberel, Sodnomsambuu

Important note
To cite this publication, please use the final published version (if applicable).
Please check the document version above.

Correspondence to:
M. J. Comeau,
M.J.Comeau@tudelft.nl

Author Contributions:
Conceptualization: Matthew J. Comeau
Formal analysis: Matthew J. Comeau, Rafael Rigaud
Investigation: Erdenechimeg Batmagnai, Shoovdor Tserendug
Methodology: Matthew J. Comeau, Rafael Rigaud
Resources: Erdenechimeg Batmagnai, Alexey Kuvshinov, Michael Becken, Sodnomsambuu Demberel
Software: Matthew J. Comeau, Rafael Rigaud, Michael Becken

Insights Into the Structure of the Mongol-Okhotsk Suture Zone, Adaatsag Ophiolite, and Tectonic Boundaries of the Central Asian Orogenic Belt (Mongolia) From Electrical Resistivity Imaging and Seismic Velocity Models

Matthew J. Comeau[1] , Rafael Rigaud[2], Erdenechimeg Batmagnai[2,3] , Shoovdor Tserendug[3], Alexey Kuvshinov[2] , Michael Becken[4] , and Sodnomsambuu Demberel[3]

[1]Department of Geoscience and Engineering, Delft University of Technology, Delft, The Netherlands, [2]Swiss Federal Institute of Technology (ETH), Institute of Geophysics, Zürich, Switzerland, [3]Institute of Astronomy and Geophysics, Mongolian Academy of Sciences, Ulaanbaatar, Mongolia, [4]Institut für Geophysik, Universität Münster, Münster, Germany

Abstract The Mongol-Okhotsk suture and the Adaatsag ophiolite belt are associated with the closure of the Mongol-Okhotsk paleo-ocean and are located within the Central Asian Orogenic Belt (CAOB) and Mongolia. The suture zone is flanked by volcanic-plutonic belts that host significant metallogenic zones, containing deposits of copper and gold. The tectonic evolution of this region is not fully understood and the lithospheric structure has been poorly studied. We analyze magnetotelluric data and generate a model of the electrical resistivity distribution across this region. Whereas the northern segment has a sharp transition from a high-resistivity upper crust to a low-resistivity lower crust, as observed beneath the Hangai Dome, the southern segment does not show this transition. A wide, low-resistivity zone (1–100 Ωm) imaged in the crust and lithospheric mantle is coincident with the Mongol-Okhotsk suture and ophiolite, revealing a clear and significant lithospheric-scale feature. Across the profile, numerous narrow, vertically oriented, low-resistivity features (1–100 Ωm) are spatially associated remarkably well with the proposed boundaries of tectonic domains. These results confirm ideas about the development of the CAOB. Some of these low-resistivity features are beneath the surface locations of large mineral zones, and likely represent fossil fluid pathways. We show congruent seismic velocity models for comparison and the results show a large-scale low-velocity anomaly (decrease of 2%–3%) that correlates with the location of the low-resistivity anomaly below the Mongol-Okhotsk suture. The geophysical results, combined with geological and geochemical data, provide insights into the structure of this region and help shed light on unanswered questions.

Plain Language Summary When the ancient Mongol-Okhotsk ocean closed, due to subduction from tectonic re-arrangement, it left the Mongol-Okhotsk suture zone and the Adaatsag ophiolite as a trace of its location. Similarly, other tectonic boundaries are hypothesized to exist from terrane accretion across the Central Asian Orogenic Belt (CAOB) and Central and Southern Mongolia, which is located between the Siberian and North China cratons. This region is also rich in economically significant copper and gold deposits. The tectonic evolution of this region and especially the lithospheric structure is not fully understood and has been poorly studied. We analyze magnetotelluric data and generate a model of the electrical resistivity distribution. Additionally, we show models of the seismic velocity for comparison. Examining multiple complementary geophysical models helps to reduce interpretation uncertainty. Anomalies are observed in both models (e.g., low resistivity and low velocity). The suture zone is proven to be a strong lithospheric-scale boundary. The proposed boundaries of tectonic domains are also imaged, confirming ideas about the development of the CAOB, and solving some controversies.

1. Introduction

1.1. Study Motivation and Unanswered Questions

The Mongol-Okhotsk suture zone, formed during the final closure of the Mongol-Okhotsk paleo-ocean, is a boundary located in the center of the Central Asian Orogenic Belt (CAOB) and central Mongolia. It contains the Adaatsag ophiolite belt, which helps constrain the evolution, dynamics, and location of the final closure of the ancient ocean. Adjacent to this, volcanic–plutonic belts host economically important metallogenic zones that

Visualization: Matthew J. Comeau, Rafael Rigaud

Writing – original draft: Matthew J. Comeau

contain deposits of copper and gold (Tomurtogoo et al., 2005). However, the crustal and lithospheric structure of this region have been poorly studied.

In this study we aim to shed light on the structure, extent, and location of tectonic boundaries across central Mongolia, including the Mongol-Okhotsk suture zone, which are not always agreed upon (e.g., Kröner et al., 2010). In addition, we aim to determine variations in the properties of the lithosphere across this region. This can be used to assess whether there exists evidence for mantle plumes, as some authors suggest (e.g., Zhang et al., 2017), to determine whether lower crustal conductors observed to the west below the Hangai Dome region extend to this region, and to investigate whether clear links are visible from mineral deposits at the surface to features in the lower crust or lithosphere.

To do this, we first analyze data acquired with magnetotelluric (MT) measurements and then generate a model of the electrical resistivity distribution of the subsurface beneath this region. Afterward, we compare with congruent seismic models for S-wave and P-wave velocities. Examining multiple geophysical models, which image distinct physical parameters, helps reduce interpretation uncertainty. In particular, electrical resistivity and seismic velocity are complementary parameters, which are sensitive to subsurface rock properties such as composition, mineralogy, and fluid content, and can provide information about lithosphere-scale features. We combine the geophysical models with geological and geochemical data to help strengthen the interpretation of the results.

1.2. Tectonic and Geological Background of Study Area

1.2.1. The Central Asian Orogenic Belt and Central Mongolia

The CAOB is a long-lived accretionary orogeny (possibly the largest worldwide) that covers parts of Central and Eastern Asia (e.g., Yin, 2010) and includes large areas of central Mongolia (Figure 1a). This area is unique because it is located in the continental interior, very far from (current) major tectonic margins (Figure 1b). The Siberian craton, which is considered to be relatively stable (e.g., Calais et al., 2003), is located to the north, and the North China (Sino-Korean) and Tarim cratons (e.g., Yin, 2010) are located to the south.

The tectonic evolution of the central Mongolian part of the CAOB is complex and is very controversial (e.g., Kovach et al., 2013; Kröner et al., 2010). It formed through multiple accretion, subduction, and collisional events, largely driven by the re-organization and closure of the Paleo-Asian Ocean, and possibly in a punctuated way (Buchan et al., 2001; Kröner et al., 2010). As a result, it is composed of many different lithotectonic units (Precambrian to Triassic age). This can be clearly observed in southern Mongolia, where an accretionary collage of many ribbon-like, east-west trending lithostratigraphic provinces have been mapped. Badarch et al. (2002) distinguished 44 independent terranes or lithostratigraphic domains across Mongolia (some narrower than 25 km across), whereas Kröner et al. (2010) preferred larger lithotectonic blocks. Attempts to map these domains by their (surface) properties with different techniques, such as with structural geology, geochronology, and (aerial) potential field measurements, have led to some disagreements about the locations of domain boundaries, as well as the number of domains (Badarch et al., 2002; Guy et al., 2014; Kröner et al., 2010). Instead, identifying the significant boundaries that are reported to separate lithotectonic units, such as faults, suture zones, and tectonic boundaries, which are potentially crustal-scale or lithospheric-scale (e.g., Badarch et al., 2002; Calais et al., 2003) and which may be rheological weak zones, can be a better approach (Comeau, Becken, Käufl, et al., 2020). Geophysical techniques that are capable of imaging both shallow and deep structures are thus well suited for this task.

1.2.2. The Mongol-Okhotsk Suture Zone

The Mongol-Okhotsk suture zone was formed from the closure of the Mongol-Okhotsk paleo-ocean. The ocean existed, in the Paleozoic and Mesozoic eras, between the Siberian and Amurian (Mongolian) plates. The ocean was closed by subduction. In the modern day, the suture zone, which is the youngest part of the CAOB, runs approximately south-west to north-east and stretches for more than 3,000 km across central Mongolia (south of the Hangai–Hentei mountains), through Transbaikalia and the Amur river region, and to the Sea of Okhotsk and the western Pacific Ocean (Tomurtogoo et al., 2005; Van der Voo et al., 2015). Within Mongolia, an accretionary wedge is identified to the north of the suture zone (Hangai–Hentei basin) (Badarch et al., 2002). Flanking the suture zone for much of its length is an immense region (hundreds of kilometers wide, on each side) of Devonian–Cretaceous volcanic–plutonic belts (e.g., in Mongolia, the Selenge belt to the north and Middle Gobi belt to the
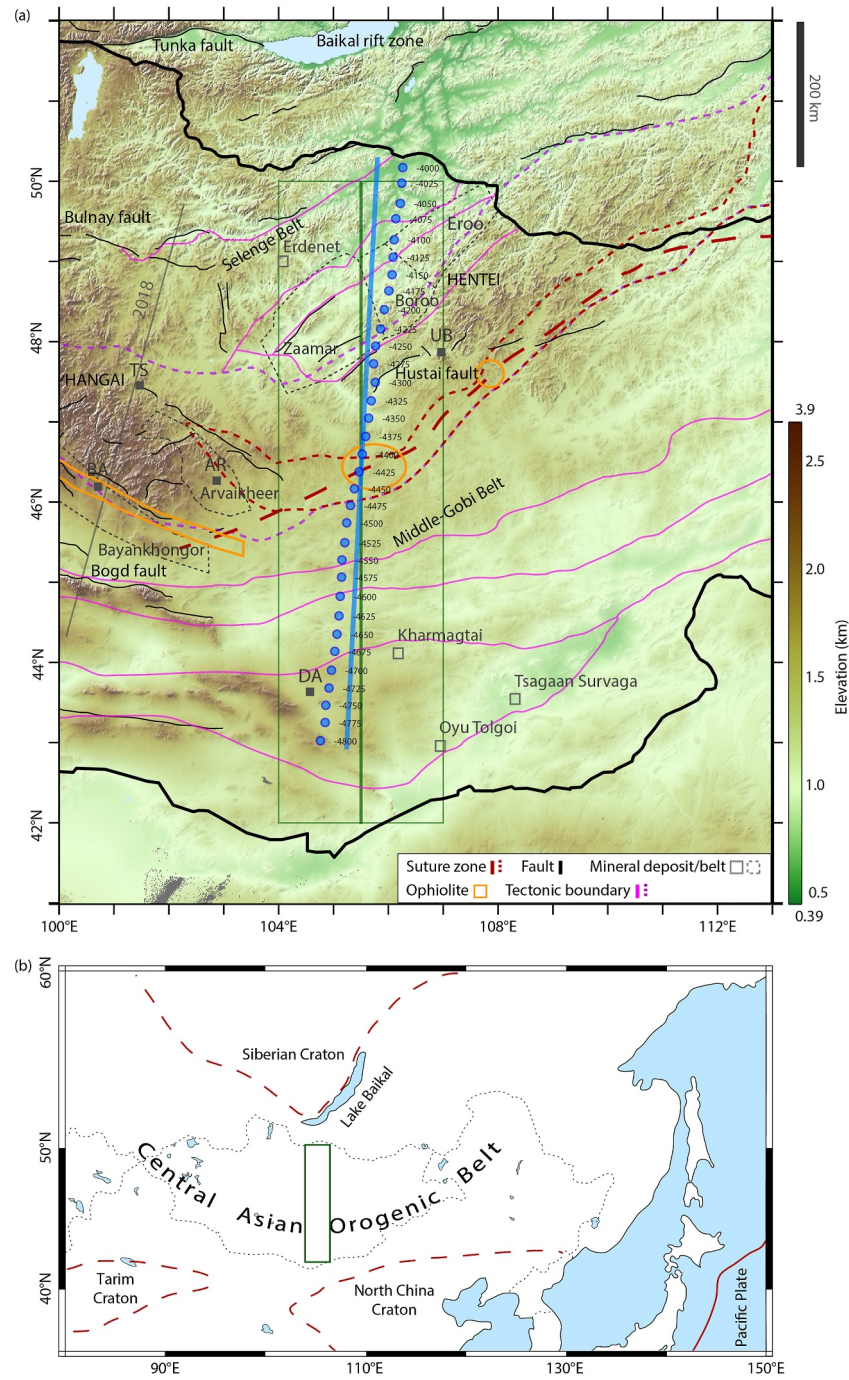
Figure 1.

south) and mineralization (Dergunov, 2001; Van der Voo et al., 2015). The metallogenic zones associated with these belts include copper-molybdenum deposits, gold deposits, and porphyry copper-gold-molybdenum deposits (e.g., Dergunov, 2001; Singer et al., 2008; Tomurtogoo et al., 2005).

The timeline and style of closure for the Mongol-Okhotsk paleo-ocean is debated. It is often assumed to have been in the Late Jurassic or Early Cretaceous (Tomurtogoo et al., 2005; Van der Voo et al., 2015), and geochronology and geochemistry offer similar estimates to paleomagnetic data. Based on paleomagnetic analysis, Van der Voo et al. (2015) suggested that the final closure occurred between 160–120 Ma, from west to east with a scissor-like closure mechanism that caused doubly vergent subduction, necessary to explain why it is not well identified west of longitude ~98°E and appears to terminate without connection to other plate boundaries. Kravchinsky et al. (2002) calculated that the rate of closure, at the end of the Jurassic, averaged 13.3 cm per year.

The Mongol-Okhotsk suture zone includes several significant ophiolite belts (Buchan et al., 2001; Tomurtogoo et al., 2005). Ophiolite belts, exposed regions where a sequence of oceanic lithosphere was thrust over a continental margin, are important because they can provide evidence for the location and age of the subduction and closure of paleo-oceans (e.g., Dilek & Furnes, 2014). The Adaatsag ophiolite belt is found within the Mongol-Okhotsk suture zone, approximately 180 km south-southwest of Ulaanbaatar. Isotopic data from zircon grains indicate a mean age of ~325 Ma ($^{207}Pb/^{206}Pb$; Tomurtogoo et al., 2005). This implies that new oceanic crust was being generated at this time (i.e., active seafloor spreading).

1.2.3. Geodynamic Implications

Tomurtogoo et al. (2005) searched for a tectonic model that could explain the observed features and history of the Mongol-Okhotsk belt, including the post-collisional alkaline magmatism. One hypothesis that they considered was that after prolonged subduction processes either slab break-off or the delamination of a thickened and unstable lithosphere would result in upwelling of hot asthenosphere and decompression melting (ultimately generating widespread alkaline basaltic magmas).

Dehydration melting from subducting oceanic plates, including from previous events in the CAOB before the formation of the Mongol-Okhotsk region, would have hydrated the lithosphere and led to (alkaline) metasomatism of the lithospheric mantle (Tomurtogoo et al., 2005). This may have established conditions in the region for a subsequent delamination event (see Comeau et al., 2021; Stein et al., 2022; Tomurtogoo et al., 2005). In fact, geochemical data indicate that metasomatism of a hydrated lithosphere likely occurred beneath parts of Mongolia near the Mongol-Okhotsk suture zone (Sheldrick et al., 2020). Furthermore, thermo-mechanical numerical modeling has shown that deep (lithospheric-scale) faults or sutures, which may have significantly different properties (e.g., rheological and chemical) from the surrounding regions (e.g., Jin et al., 2022), can act to focus deformation and are therefore important initiation points for detachment of the lithosphere (Comeau et al., 2021; Stein et al., 2022).

Using S-wave receiver functions, Zhao et al. (2021) interpreted a broken lithosphere–asthenosphere boundary (due to upwelling) and delaminated lithosphere at a depth of 200–300 km below the Mongol-Okhotsk suture zone (approximately at 105°E and 46°N). Based on global seismic tomography images, Van der Voo et al. (2015)

Figure 1. Map of the study area. (a) Measurement locations for magnetotelluric sites are labeled and marked (blue circles). The projected profile is drawn (blue line). It is approximately along longitude 105.5°E. The northern-most site has coordinates of 106.26°E, 50.17°N; the southern-most site has coordinates of 104.76°E, 43.03°N. For context, a profile across the Hangai Dome, 300–400 km to the east, by Comeau et al. (2018) is marked (gray line). The location of a near-coincident seismic section along 105.5°E is indicated (green line) and the seismic model area in Section 3.2 is marked (green box). The proposed location of the Mongol-Okhotsk suture zone is drawn from Tomurtogoo et al. (2005) (long-dash red line) and Zhao et al. (2017) (dashed red line). The location of the Adaatsag ophiolite is indicated with an orange ellipse (center; Tomurtogoo et al., 2005); the Bayankhongor ophiolite is outlined with an orange polygon (Badarch et al., 2002); the Khuhu Davaa ophiolite is marked with a small orange circle (Zhu et al., 2023). The proposed location of an accretionary wedge (Hangai–Hentei basin) is drawn (dotted purple line) from Zhao et al. (2017). Significant tectonic boundaries in Mongolia are drawn, believed to be from accreted terranes or different lithotectonic units (pink lines; based on Badarch et al. (2002) and Guy et al. (2014)). Important mineral zones are marked, including the Eroo, Boroo, and Zaamar gold belts that cross the northern part of the profile and the Arvaikheer and Bayankhongor gold belt to the west (gray dotted outline; Dejidmaa, 1996), as well as the Erdenet copper district and the Oyu Tolgoi, Kharmagtai, and Tsagaan Survaga copper and gold districts (gray squares; Mineral Resources Authority of Mongolia, 2014; Singer et al., 2008). The surface traces of fault zones are marked (black lines; from the database of Styron (2018), with additions from Calais et al. (2003), Walker et al. (2007), and Zhao et al. (2021)). The political boundary of Mongolia, as well as selected towns are labeled for reference (Ulaanbaatar (capital city): UB; Arvaikheer: AR; Erdenet: ER; Tsetserleg: TS; Bayankhongor: BA; Dalanzadgad: DA). (b) Regional map. The study area (indicated with the green box) sits within the Central Asian Orogenic Belt. The Siberian craton, the North China craton and Tarim craton, and the Pacific plate are marked.

attempted to locate the remnants of the ancient subducted slab of ocean lithosphere from the closure of the Mongol-Okhotsk ocean, and determined it was farther west in the lower mantle and stagnating in a slab graveyard.

1.2.4. Adjacent Metallogenic Zones

This region contains economically important mining zones. At the northern end of the study area the Erdenet copper-molybdenum mine (age of ~230 Ma; 2,370 Mt; 0.7% Cu, 0.013% Mo; <0.07 g/t Au) (Singer et al., 2008) is located. Nearby are the Zaamar, Boroo, and Eroo gold belts, part of the North Hentei gold belt. This region is part of the Haraa terrane (Badarch et al., 2002), which is bounded by large faults that extend for hundreds of kilometers north-east into the Transbaikal region, with the Yeroogol fault to the south and to the north the Bayangol fault and edge of the Bayangol terrane. Boroo is a hard rock intrusion-related gold deposit hosted in strongly altered quartz veins (with sulphide) controlled by the Boroo thrust fault (Dejidmaa, 1996). Khishgee and Akasaka (2015) classified it as orogenic type, determined an age of 210–185 Ma, and estimated grades of 1–10 g/t Au.

At the southern end of the study area, several large porphyry copper-gold-(molybdenum) deposits exist, including Oyu Tolgoi (age of ~367 Ma; 3,107 Mt; 0.7% Cu, 0.24 g/t Au), Kharmagtai (age of ~330 Ma; 228 Mt; 0.4% Cu, 0.3–2.5 g/t Au), and Tsagaan Survaga (age of ~370 Ma; 240 Mt; 0.5% Cu, 0.018% Mo; 0.084–2.6 g/t Au) (Singer et al., 2008). Dejidmaa (1996) classified these as intrusion related deposits in an active continental margin, and Sillitoe et al. (1996) noted that these deposits are associated with magmatic complexes of elevated alkalinity (e.g., total alkali oxide content, $Na_2O + K_2O$, near 9%).

2. Methods

2.1. Magnetotelluric Data Acquisition

The MT method is an electromagnetic geophysical technique used to image the subsurface electrical resistivity distribution (e.g., Cagniard, 1953). It makes use of natural-source electromagnetic signals that are generated in the atmosphere and ionosphere (e.g., Simpson & Bahr, 2005; Unsworth & Rondenay, 2012). The electric and magnetic field variations at the Earth's surface are measured over a broad range of periods. This gives sensitivity to multiple spatial scales: long-period data are sensitive to great depths and short-period data are sensitive to shallow depths. However, because the MT method is a volume sounding method, data at measurement locations are influenced by both structures beneath the site and around the site (e.g., Simpson & Bahr, 2005). The electric and magnetic field variations are related by a (complex-valued) impedance tensor ($\mathbf{Z}$), or transfer function, from which the apparent resistivity (ρ), as well as the impedance phase (φ), can be determined. In addition, the ratio of the horizontal and vertical magnetic fields, known as the tipper, gives complementary information and can be included in analysis and modeling.

MT data are especially sensitive to the quantity and composition of low-resistivity materials in the subsurface, such as fluids, when they are interconnected (rather than isolated). The MT technique is well-suited to image the structure of fault zones, as well as suture zones and tectonic boundaries, which are regions of deformed and/or weakened and fractured crust due to past tectonic activity (with implications for rheology), in addition to other lithospheric structures (e.g., Heinson et al., 2005; Sheng et al., 2021; Türkoğlu et al., 2008; Wang et al., 2022; Wannamaker et al., 2002, 2008).

In summer 2022, from the 15th of June to the 8th of July, a profile of MT measurements was acquired across central Mongolia (named profile −4000). The profile contains 34 measurement sites and has a typical spacing of ~25 km between sites. The profile extends a total of ~810 km, north to south, approximately along a longitude of 105.5°E (the northern-most site had coordinates of 106.26°E, 50.17°N; the southern-most site had coordinates of 104.76°E, 43.03°N). The profile is shown on the map in Figure 1. It is located 300–400 km east of a profile across the Hangai Dome described by Comeau et al. (2018) (named profile +2000) and more than 250 km east of an array across west-central Mongolia described by Käufl, Grayver, Comeau, et al. (2020). Newly acquired data across central Mongolia fills the gaps between the above-mentioned profiles (Rigaud, Comeau, Becken, et al., 2023; Rigaud, Comeau, Kuvshinov, et al., 2023).

The perpendicular horizontal components of electric and magnetic fields (which were aligned along the north-south and east-west directions), were continuously recorded with a 500 Hz sampling frequency. In addition, at most locations, the vertical magnetic field was measured; however it is not considered in this study. This study
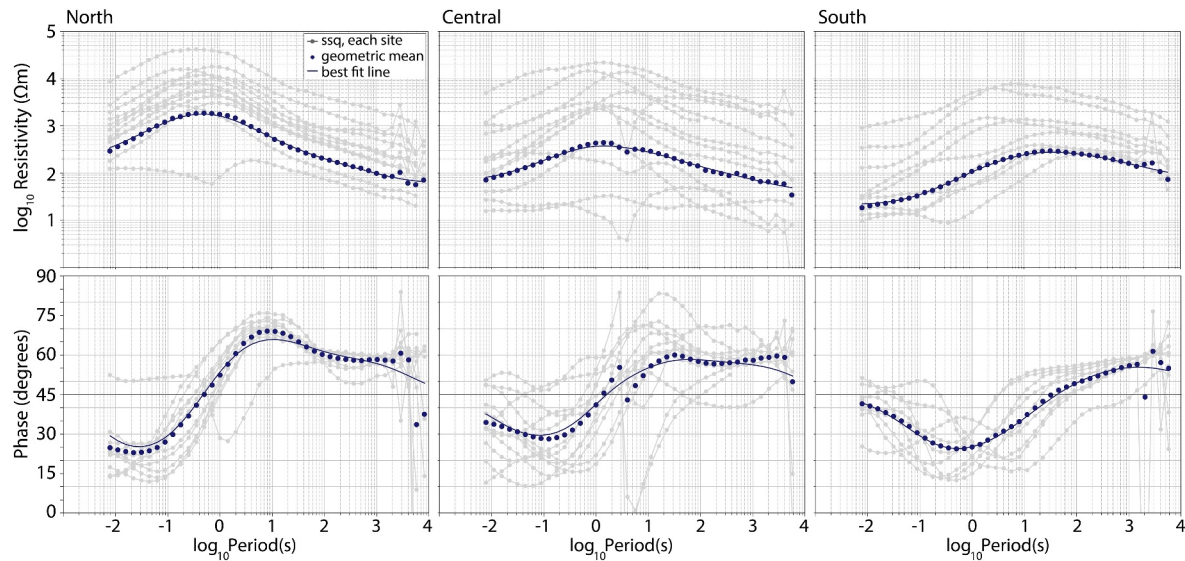
Figure 2. Observed magnetotelluric data. Apparent resistivity (top) and phase (bottom) plotted against period, from the computed SSQ impedances (square root of the sum of the squared elements of the impedance tensor; Rung-Arunwan et al., 2016) for all measurement locations (gray dots and lines). The geometric mean is shown (blue dots) as well as the best fit line (blue). To highlight differences, the profile is divided into three segments: north (sites 4000–4275), central (sites 4300–4575), and south (sites 4600–4800).

used the following equipment: LEMI-423 wideband magnetotelluric data logger in combination with LEMI-120 broadband induction coil magnetometers and LEMI-701 non-polarizing porous-pot electrodes with a copper-copper sulfate (Cu–CuSO$_4$) electrolyte. Whenever possible, an electric dipole length of 60 m was used.

Measurement site occupation times were typically 3–4 days (2–3 nights). At most sites, reliable data were recorded up to a period of 4,096–5,793 s (six sites achieved up to 8,192 s). In general, the data had a very low noise level and were good quality, attributed to the remote measurement location and lack of dense infrastructure and man-made electromagnetic signals.

2.2. Magnetotelluric Data Analysis

2.2.1. Examining Apparent Resistivity and Phase

Careful processing of the MT data was undertaken, including converting the raw time series (field observations) into the frequency domain and computing robust estimates of the impedance tensor as a function of frequency for each measurement location (Becken et al., 2014). For each individual measurement site, the processing parameters were manually selected, including the time window, the bi-coherence threshold values, and whether remote reference processing was required to minimize noise. This was done to ensure high quality and to maximize the period range of the computed transfer functions.

A cursory look at the data, plotted in terms of apparent resistivity and phase curves (against period or frequency, a proxy for depth), revealed differences along the profile. In order to gain insights into the data they were divided into three segments: north (sites 4000–4275; note that the three last digits in the site name indicate the distance in kilometers from the northern-most site), central (sites 4300–4575), and south (sites 4600–4800). For each of the MT sites the SSQ impedance was computed (which is the square root of the sum of the squared elements of the impedance tensor; Rung-Arunwan et al., 2016). Examining the apparent resistivity curves, large static shifts are observed (Figure 2). These are up to 1–2 orders of magnitude in the central region. Static shifts are constant (period-independent) shifts of the apparent resistivity that are caused by the near-surface and small features (e.g., Simpson & Bahr, 2005). The geometric mean was calculated for each segment (which averages out the effect of static shifts) and a best fit line was computed.

The analysis clearly shows that the character of the electrical resistivity is distinct in the southern region. Looking at the shape of the phase curves (i.e., phase against period), which were fairly consistent, one notices that in the northern segment the phase curves are 10–30° at a period of 0.01 s, increase to 70° at 10 s, and decrease to 60° at
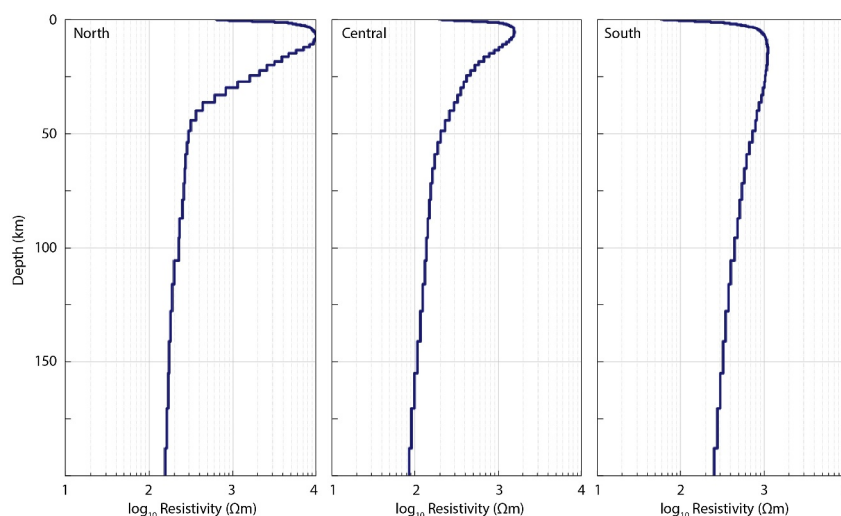
Figure 3. A 1-D electrical resistivity model, for each segment of the profile. The model was generated from the geometric mean of the SSQ impedances in each segment with the algorithm of Grayver and Kuvshinov (2016). The differences between the models for each segment are clear, with the southern part being quite distinct.

1,000 s. There is one exception to this trend, which is the northern-most site (site 4000). The apparent resistivity curves decrease (more than one order of magnitude) from a peak at a period of 0.1–1 s. In contrast, in the southern segment the phase curves, which were very tightly clustered, are 40–50° at a period of 0.01 s, decrease to 10–30° at 1 s, and increase to 60° at 1,000 s. The apparent resistivity curves are, in comparison, somewhat flat (decreasing only half an order of magnitude) and the peak is shifted toward a period of 10–100 s. In the central region the phase curves had much variability, but the general shapes were transitioning between those described above for the northern and southern regions. Some sites had very high phases for one mode, typically from 1–10 s, up to 80–90° (sites 4350 and 4475) or greater than 90° (i.e., leaving the quadrant; sites 4300 and 4425).

A similar difference was noted in west-central Mongolia across the Hangai Dome and Gobi-Altai, for a profile located 300–400 km to the west (see Comeau, Becken, Käufl, et al., 2020; Comeau et al., 2018). There, in the northern and central areas the phase curves typically range from 20 to 40° at a period of 0.01–0.1 s, increase to 70–80° at 10 s, and decrease to 50–60° at 1,000 s; the apparent resistivity curves decrease (more than one order of magnitude) rapidly from a peak at 0.1–1 s (corresponding to a decrease in the middle-lower crust). Whereas in southern Mongolia near the Gobi-Altai the phase curves are typically about 45° at a period of 0.01 s, decrease to 10–40° at 0.1–1 s, and increase to 50–60° at 100 s; the apparent resistivity curves are fairly flat, decreasing less than half an order of magnitude from a peak near a period of 10 s. This similarity is an indication that the regional tectonic structure in the north of both regions (west-central and central Mongolia) is consistent and distinct from the regional tectonic structure in the south of both regions.

2.2.2. One-Dimensional Modeling and Penetration Depth Estimates

For each profile segment (north, central, and south), a simple one-dimensional (1-D) electrical resistivity model was computed from the geometric mean of the SSQ impedances (Figure 3), using the algorithm of Grayver and Kuvshinov (2016). It clearly shows that the character of the electrical resistivity is distinct in the southern region. In the northern region, the upper crust (0–25 km) is highly resistive, up to 10,000 Ωm, and the lower crust (25–45 km) is about 300–1,000 Ωm. The central region is similar (about 2,000 Ωm in the upper crust and 200 Ωm in the lower crust). In the southern region the entire crust is about 800–1,000 Ωm and is much more homogenous. The character of the northern region is similar to that described by Comeau et al. (2018) below the Hangai Dome, 300–400 km to the west: a strong and sharp contrast (∼1.5 orders of magnitude) between the upper and the lower crust, although the very low resistivity observed throughout the lower crust (30–100 Ωm) below the Hangai Dome is not observed here.

To gain an idea about what depths the electromagnetic data are sensitive to, the average penetration depth was estimated from the real part of the C-response (from the geometric mean of the SSQ impedances), as discussed by
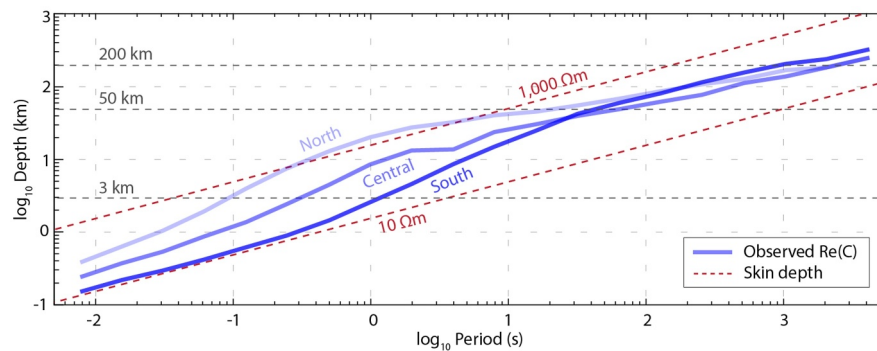
Figure 4. Estimate of the electromagnetic penetration depth. The real part of the C-response is computed for each segment of the profile (north, central, and south; solid blue lines), based on the geometric mean of the data in each segment. Simple penetration depth estimates based on the skin depth for a (homogenous) halfspace of 10 and 1,000 Ωm are shown (dotted red lines).

Weidelt (1972). Note that this approach is less accurate for non 1-D parts of the profile (e.g., Jones, 2006). The analysis (Figure 4) shows that the data have good sensitivity to crustal depths and to upper mantle depths. For example, in general, periods of less than 0.1 s penetrate to depths of less than 3 km, periods of 1 s penetrate to depths of 3–20 km (upper crust), periods of 30 s penetrate to depths of 40–50 km (the crust–mantle boundary), and periods greater than 1,000 s penetrate to depths of 150–200 km (into the upper mantle and possibly the asthenosphere). The penetration depth is deeper in the northern region than in the southern region for short periods, for example, at 1 s a 20 km penetration compared to a 3 km penetration, which is reflective of the very high resistivity in the upper crust of the northern region. All regions show similar penetration depths for long periods, for example, above 30 s.

2.3. Magnetotelluric Directionality and Dimensionality Analysis

2.3.1. Tensor Decomposition

Careful analysis of the data is required to determine if a two-dimensional (2-D) electrical resistivity model is generally suitable or if a three-dimensional (3-D) model is needed. The tensor decomposition method of Groom and Bailey (1989) was used by applying the algorithm of McNeice and Jones (2001). Because the electric field can be perturbed by local charge distributions, quantifying the distortion is useful. The shear and twist are two parameters (sub-tensors) that (partially) describe the effects of telluric distortion. In the data presented here, they mostly ranged between ±30° and ±20°, respectively. Estimates for the geo-electric strike direction at each site were binned into a circular histogram (rose diagram) to given an idea of the overall distribution. For a broad range of periods, 1–4,096 s, a clearly defined geo-electric strike direction is observed (Figure 5a), with a dominant angle of N90°E–N100°E (note that an inherent 90° ambiguity exists) and a secondary peak of ~N40°E–N60°E.

Looking a smaller period bands reveals interesting results. At periods less than 1 s (upper crust), a clear direction of N90°E–N100°E is observed; periods of 1–10 s (e.g., upper to lower crust) show a significant amount of scatter, possibly indicating a transition in the strike angle upon entering the (heterogeneous) lower crust, but a direction of N90°E–N100°E still dominates; periods of 10–100 s (e.g., middle crust to upper mantle) show a primary peak of N90°E–N100°E and a secondary peak of ~N40°E–N60°E; periods of 100–1,000 s (e.g., upper mantle) show a primary peak of N90°E–N100°E and a secondary peak of N50°E–N70°E.

These determined geo-electric strike angles are not unexpected; they are consistent with the general trend of tectonic features in this part of Mongolia (see map in Figure 1). Generally speaking, west of the profile tectonic/geological domains are oriented west-east or north-west to south-east, and east of the profile they are oriented south-west to north-east. The angles are consistent with the range determined for MT data in west-central Mongolia (N90°E–N120°E; Comeau, Becken, Käufl, et al., 2020; Comeau et al., 2018). Further analysis was carried out to pick one single strike angle that best satisfies all the data (by examining the misfit of each site and all sites as the data are rotated through various angles; following Comeau et al. (2016)), which gives a preferred angle of N93°E. In addition, the misfit at each site and each period of the measured impedance
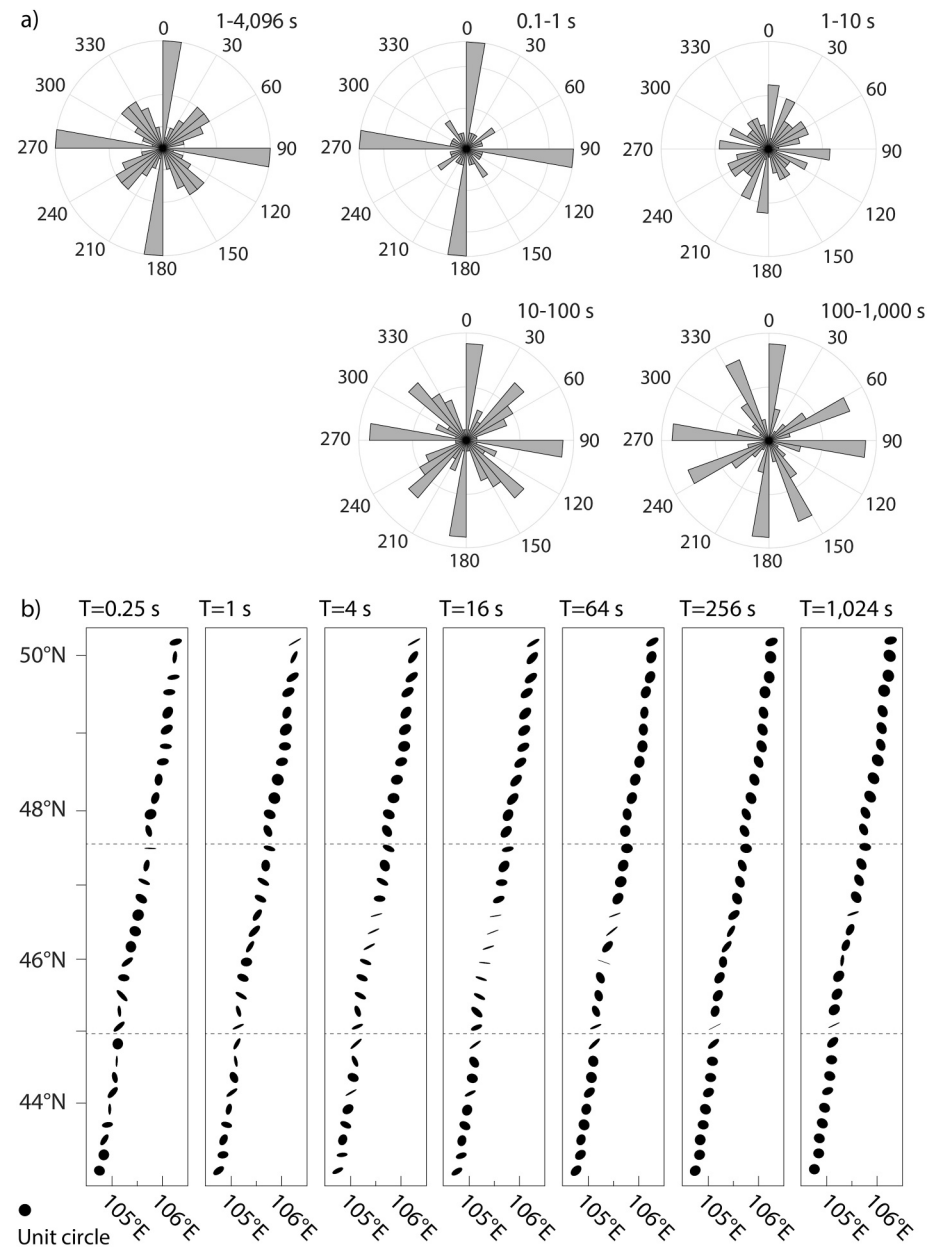
Figure 5. Directionality analysis of the data. (a) The geo-electric strike direction is estimated from the tensor decomposition method (Groom & Bailey, 1989; McNeice & Jones, 2001) and is shown with circular histograms. Periods of 1–4,096 s show an overall geo-electric strike direction of N90°E–N100°E. In some individual period bands a secondary peak is revealed. Radial bins are counts of five. (b) Phase tensor ellipses are shown in map view. Increasing periods correspond to increasing depths. For 1-D geo-electric structure, the phase tensors are expected to be circular in shape. For 2-D structure, the axes of the phase tensors are expected to align with the along and across geo-electric strike directions The profile is divided into three segments (dashed gray lines).

to the values predicted by the tensor decomposition method for the chosen strike angle are examined (Figure S1 in Supporting Information S1) and reveal that the strike angle does not fit well between N46°E–N46.5°E (profile distance of 400–450 km) and at short periods near N45°E (profile distance of 550–600 km), associated with the location of the ophiolite and a significant terrane boundary (see map in Figure 1), but that the strike angle does fit well overall.
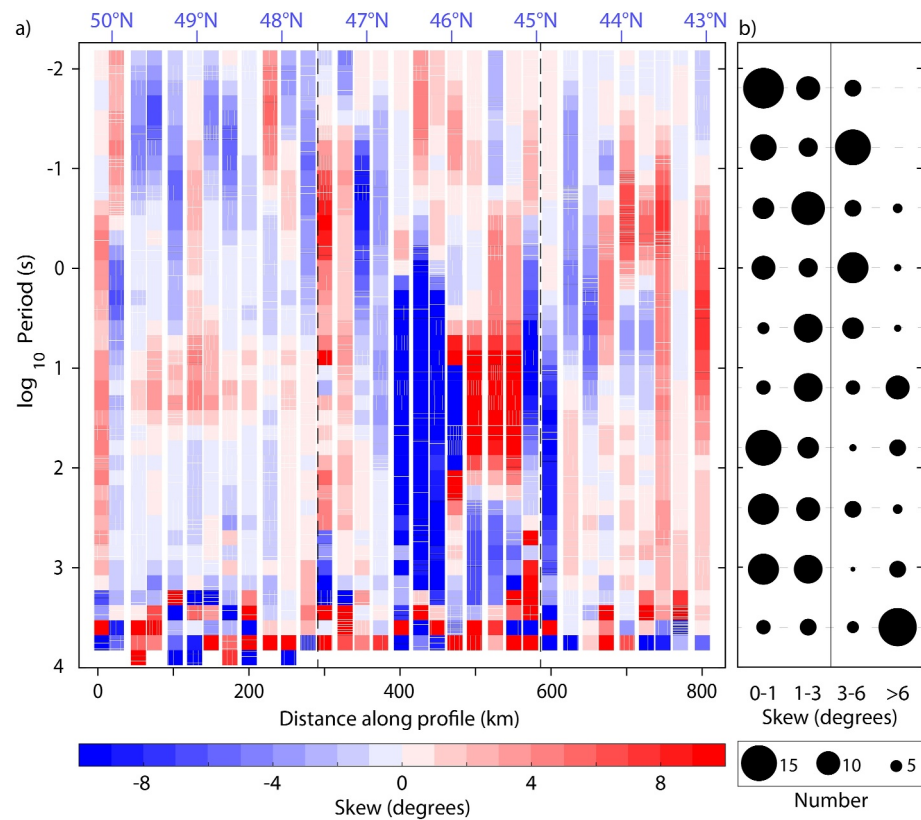
Figure 6. Dimensionality analysis of the data. (a) Phase tensor skew values are shown in pseudo-section format, plotted along the profile with period. Orientation is north to south (site 4000 on the left and site 4800 on the right). Low absolute skew values (<3°) indicate relatively 2-D data. The profile is divided into three segments (dashed gray lines, at about distances of ~300 and ~600 km). (b) The distribution of (absolute) skew values across selected periods (e.g., 0.25, 1, 4, 16, 64, 256 s, etc.). The number of skew values in each bin (total is 34 for each period) is shown with a proportionally sized circle (radius). The majority of points have absolute skew values ≤3°. For the longest periods, lower-quality data can cause the skew values to be higher.

2.3.2. Phase Tensor Analysis

A second method, phase tensor analysis, was used to verify the directionality of the MT data (Figure 5b). The phase tensor is commonly represented with an ellipse (Booker, 2014; Caldwell et al., 2004) with the axes parallel to the directions of greatest and least inductive response (which is equivalent to along and across the electric strike direction when assuming 2-D models, and a skew angle of 0°; Bibby et al., 2005). The phase tensor is not affected by galvanic distortions, including static shifts. Looking at the ellipses in map view shows that the majority are near-circular but some regions do display a strong direction. This is particularly true at ~N46°E–N47°E and near N45°E (profile distances of ~400–500 and 600 km, respectively) for the period range of 4–64 s (e.g., approximately 20–50 km depths). Interestingly, it is exactly these locations that have significant tectonic boundaries (see map in Figure 1). The directions vary, with south-west to north-east, west-east, and north-west to south-east directions observed (e.g., N60°E–N120°E). This is consistent with the tensor decomposition method. It is interesting to consider the different ways in which the tensor decomposition method and the phase tensors are responding to the data.

In addition, the skew angle of the phase tensor can help to indicate 3-D effects (Caldwell et al., 2004); large-magnitude skew values, such as greater than 6°, indicate significant 3-D effects, whereas low-magnitude values, such as 3° or less, imply that a 2-D assumption of the Earth may be reasonable. A pseudosection of the phase tensor skew for all data is presented in Figure 6a and a summary of the distribution of skew values across periods is shown in Figure 6b. Along the profile examined in this study, most absolute skew values are low (32% are 1° or less, 62% are 3° or less, and 82% are 5° or less), with large values (approximately 11% are above 6° for periods less than 1,000 s). However, some regions do display higher magnitude values, due to distortion and/or

local (3-D) structure. This is particularly true between ~N45°E–N47°E (profile distances of ~400–600 km; see map in Figure 1 and note these correspond to major tectonic boundaries) for the period range of 4–128 s, where simple 2-D structures may struggle to fit the data.

Overall, the phase tensor analysis supports the assumption of a 2-D model. Of course this assumption (that the electrical resistivity structure does not vary at all perpendicular to the profile but only along it) is a simplification; thus it is possible that some aspects of the final 2-D model may be affected by distortion effects. Following these results, the data were mathematically rotated to the preferred electric strike direction (N93°E) and were then projected onto a perpendicular profile (N3°E) for 2-D modeling. Note that the orientation of the actual collected profile was N7.7°E.

2.4. 2-Dimensional Modeling

A 2-D electrical resistivity model was generated with the MARE2DEM (Key, 2016) inversion algorithm from the MT data along the profile. We used 39 periods, logarithmically spaced from 0.0078 to 4,096 s, and 34 measurement locations. Both modes of the impedance tensor were inverted (the off-diagonal components). This consists of the transverse magnetic (TM) mode with electric currents flowing in the profile direction and the transverse electric (TE) mode with electric currents flowing in the geo-electric strike direction (i.e., perpendicular).

The starting model was chosen to be a homogenous halfspace with a resistivity of 100 Ωm. The modeling mesh (Figure 7), which consisted of triangular elements, was created so that the elements increased in size downwards, as follows: from the surface to 2 km depth, the elements had dimensions of 1.5 km, from 2 to 10 km depth the mesh elements had dimensions of 2 km, from 10 to 45 km depth they had dimensions of 3 km, from 45 to 90 km they had dimensions of 5 km, from 90 to 200 km they had dimensions of 10 km, and from 200 to 1,000 km their dimensions increased smoothly to a maximum dimension of 150 km. Similarly, for the horizontal direction, the mesh was kept fine along the profile and 20 km from its edges, but then expanded with mesh elements reaching a maximum dimension of 150 km at a distance of 1,000 km.

Errors in the measured data are typically very small, thus it is common practice to assign an error floor. The phase components (both TE and TM modes) were assigned an error of 1.43° (which is equivalent to 5% error on apparent resistivity). This ensures a close fit to the phase data (which are reliable and consistent between sites). The TM mode apparent resistivity was assigned an error floor of 10%, and, to account for the static shift effect, the TE mode apparent resistivity was assigned a high error floor of 100% in the first stage (adjusted to 10% in the third stage, see below for details). This allows the TE mode apparent resistivity curve to be shifted, within error, for all periods by a constant factor, but maintains the curve shape because of the closely fitted phase component. Effectively it is a down-weighting of the TE mode apparent resistivity component. Static shifts in the TM mode apparent resistivity can be partly accommodated by the inversion model, as described by Becken et al. (2008). The effects of 3-D conductive features will be strongest in the TE apparent resistivity response. This approach was used successfully for 2-D modeling in adjacent regions of Mongolia by Comeau et al. (2018) and Comeau, Becken, Käufl, et al. (2020).

Different inversion strategies were thoroughly tested, and the preferred strategy uses the following three stage scheme. In the first stage, the inversion algorithm is allowed to converge. Then, in the second stage, the target misfit is adjusted to the final misfit so that the inversion algorithm carries out the smoothing phase of the Occam algorithm, in which the model with the smallest roughness norm is sought. Typically, these two stages are sufficient. However, in addition, we carry out a third stage where a frequency-independent shift factor is computed (for each apparent resistivity curve) and where the TE mode apparent resistivity is re-assigned a 10% error floor (i.e., equal to the TM mode apparent resistivity error floor and thus no down-weighting). The static shifts are computed in MARE2DEM with a simple static shift solver that uses the mean residual from the model fit to estimate, at each site, an appropriate shift in the apparent resistivity curves.

In the first stage, the inversion algorithm converged after 10 iterations. In this stage, the total root-mean-square (RMS) misfit was reduced from 12.9 to 2.51. In the second stage (smoothing), the inversion algorithm was run for seven iterations. And finally, in the third stage, the inversion algorithm was run for two iterations until it stopped with a final RMS of 2.64 (recall that this stage had equal weight on the apparent resistivity errors). This is the final 2-D model.
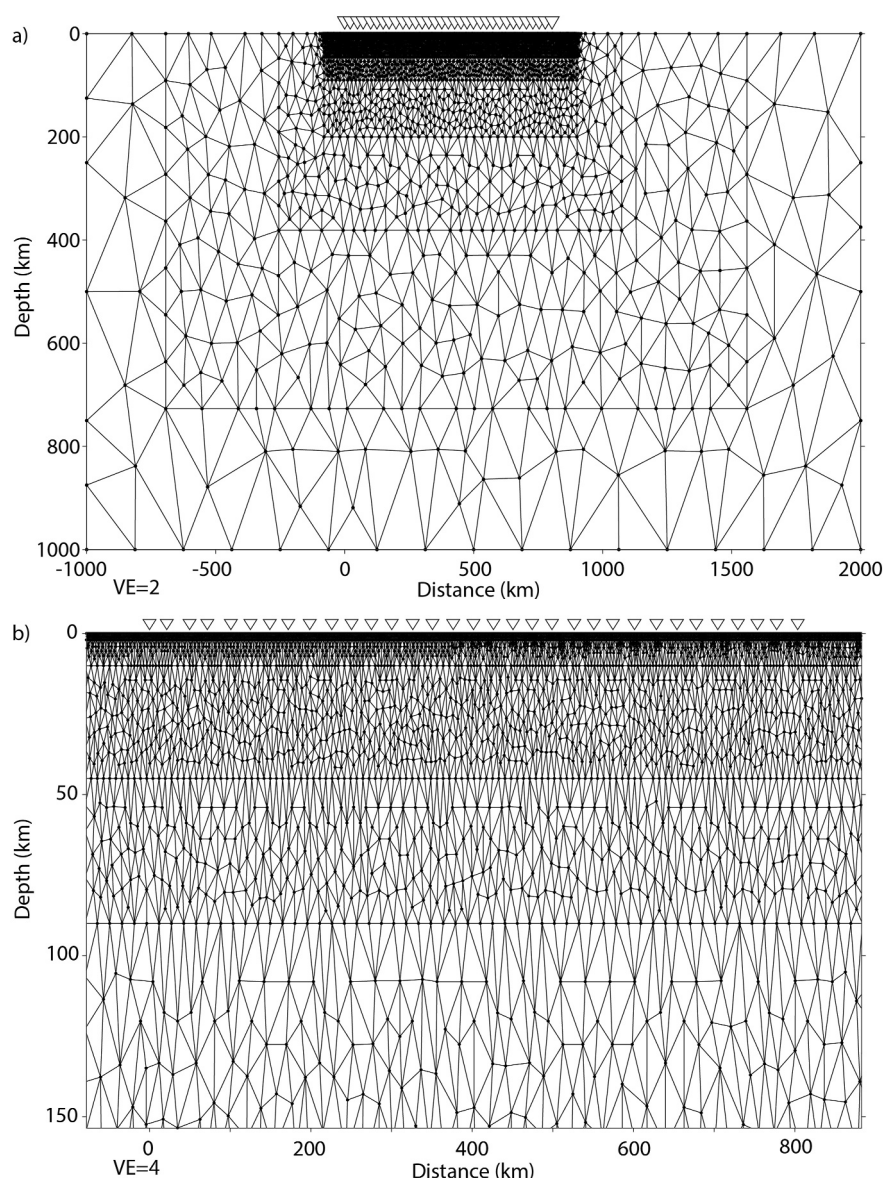
Figure 7. The modeling mesh. (a) The whole modeling area is shown. The vertical exaggeration is a factor of 2. (b) Only the core model area is shown. The vertical exaggeration is a factor of 4. Orientation is north (left) to south (right). Depth is below surface. Distance is along the projected profile (see Figure 1).

Different combinations of inversion model parameters were tested. These included adjusting the starting model halfspace (e.g., 100 or 300 Ωm), reducing the period range inverted (e.g., excluding very short periods or very long periods), modifying the data subset inverted (e.g., removing complicated data from some sites), varying the strike (e.g., ±30°), etc. Overall, the major structures and interpretable anomalies observed in the resistivity model did not significantly depend on specific parameters (for an example of varying strike angles see Figure S3 in Supporting Information S1). Thus the final model can be considered representative of those cases. Such tests can help ensure that the interpreted model features are required and robust.

In particular, two sites, one at ~300 km distance (4300) and one at ~525 km distance (4425), had out of quadrant phases, that is, phases above 90°, for periods of 1–100 s and had large magnitudes for the diagonal components. We carefully removed the data points with out of quadrant phases and used this subset in the inversion, as the 2-D inversion algorithm struggles to fit such data. For comparison, when the two measurement sites were removed completely the RMS misfit dropped (by 5%–10%) but the main model features did not substantially change.
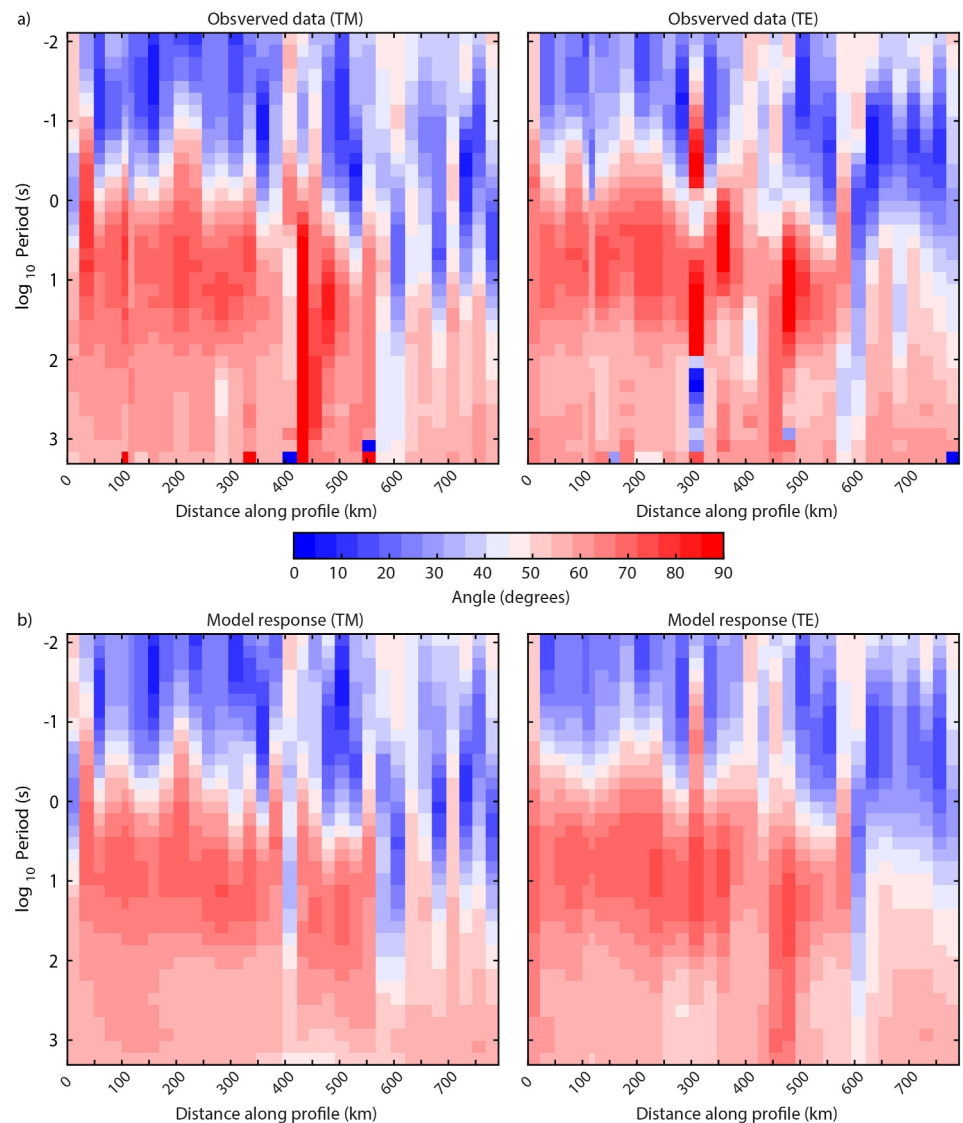
Figure 8. Data and model response, as pseudo-sections. (a) The measured phase data are shown against period (a proxy for depth) for both modes (TE and TM; Zyx and Zxy correspondingly). (b) The model responses are shown. Orientation is north (left) to south (right) and the horizontal axes show the profile distance.

Additionally, when we omitted all data above a period of 4,096 s, because they were often very scattered (noisy) although data were recorded up to a period of 8,192 s, the RMS misfit (by >10%) but the main model features did not change.

Tests were also carried out using different modeling meshes (e.g., a coarser grid, finer in shallow area only, finer everywhere, etc.). Additionally, tests were run to include topography in the model. Along the profile, the elevation varies from a minimum of 630 m above sea level (north) to a maximum of 1,900 m above sea level (south), with an average elevation of 1,300 m above sea level. This may be considered a shallow gradient, overall. However, in parts, the terrain is somewhat rugged and changes in elevation between adjacent sites can be large. The resultant models from tests that included topography showed little regional difference from those that used the approximation of no topography; furthermore, they took much longer to converge or, in some cases, did not converge. Therefore, the final model did not include topography.

Comparing the model response and the measured data demonstrates that the model responses fit the data. This is shown as pseudo-section plots for the phase in Figure 8 (the apparent resistivity data are shown in Figure S2 of the
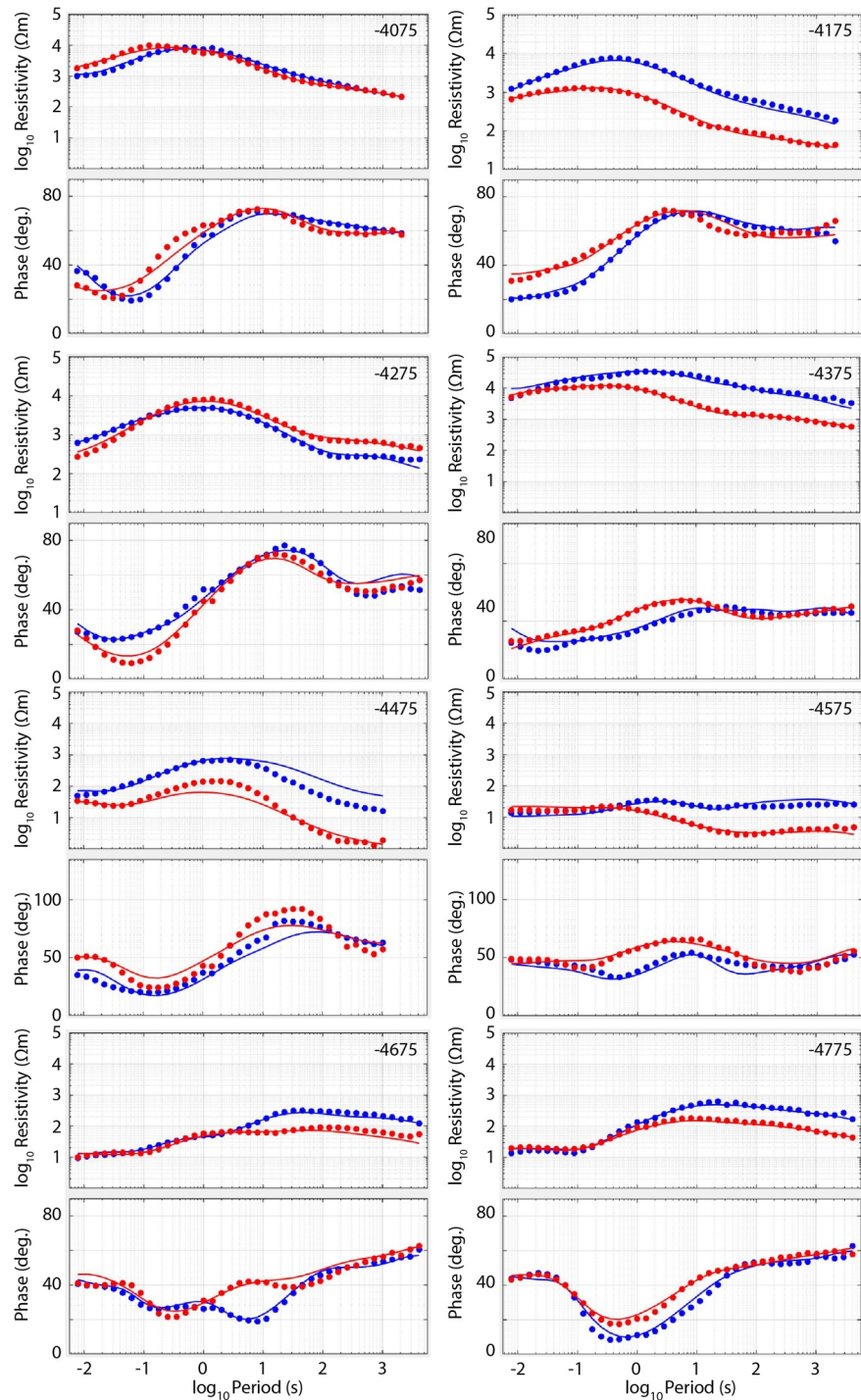
Figure 9. Data and model response from the final model, as apparent resistivity and phase curves. Selected sites equally spaced across the profile (spacing of ~100 km) are shown. The measured data are points; the model responses are lines. The model responses fit the measured data. Colors identify the two modes (blue is TE and red is TM; Zyx and Zxy correspondingly).

Supporting Information S1), and as apparent resistivity and phase curves in Figure 9. It is observed that the fit is fairly equal across all periods and across all components, which implies that the model is not more strongly influenced by certain data subsets. However, the fit of the data in the central segment of the profile was poorer (e.g., the RMS misfit ranged from 1 to 4), compared to the southern segment (range from ~1 to 2), which was the

most consistent, and the northern segment (range of ∼1 to 2.5) (shown in Figure S4 of the Supporting Information S1).

3. Results

3.1. Electrical Resistivity Model

The final 2-D electrical resistivity model, which extends ∼810 km approximately north-south, is shown in Figure 10. As observed in the MT data (Figure 2) and in the 1-D models (Figure 3), the resistivity structure is distinct in each of the three segments. In the northern region, the upper crust (from surface to a depth of ∼25 km) is highly resistive, up to 10,000 Ωm. The near-surface layer (<2,000 m) has parts that are ∼1,000 Ωm. The lower crust (depths of approximately 25–45 km) is in parts also highly resistive and in other parts moderately resistive, 300–1,000 Ωm. Previous MT studies identified a sharp transition in electrical resistivity in the mid-crust, an abrupt step-like feature that has a reduction of several orders of magnitude, which was consistent with estimates for the brittle to ductile transition depth in this region (Comeau, Becken, Connolly, et al., 2020; Käufl, Grayver, Comeau, et al., 2020). There are a few isolated regions of lower resistivity, 30–100 Ωm, centered near a depth of approximately 40 km (with an imaged width on the order of 10–30 km). At depths of 50–80 km, within the lithospheric mantle, there is a moderate resistivity of 100–1,000 Ωm. Below this, possibly in the asthenosphere, the resistivity becomes more homogenous (e.g., on the order of ∼100 Ωm).

Some pathways of 30–1,000 Ωm may connect from the lithospheric mantle or lower crust through the upper crust to the surface. Although some of the model features are subtle, they can be identified in the data (Figure 8; Figure S2 in Supporting Information S1). These features are spatially associated with the proposed boundaries of tectonic domains (see Section 4.1). Additionally, some of the anomalies are directly beneath the surface locations of large mineral provinces (copper and gold) and the projected location of the Erdenet mine (located ∼100 km west of the profile) (see Section 4.2). Measurements with a much denser spacing would be required to ensure the features are well constrained and to confirm this conclusively.

The central region shows many anomalous features. The crust has a background resistivity of 1,000–10,000 Ωm but many low-resistivity features are observed (1–100 Ωm). These features are vertically extended. The locations appear to be consistent with the proposed locations of the suture zones and ophiolite belt in this region, as well as with other fault zones (see Section 4.1). At depths of 40–80 km, within the lithospheric mantle, there is a large anomalous feature with a low resistivity of 1–10 Ωm (with an imaged width of approximately 50 km). It extends to depths greater than ∼120 km, with a resistivity of 1–30 Ωm. It must be considered that the vertical extent of the conductive features to great depths (e.g., 120–160 km) may be due to the model regularization (i.e., smoothing) rather than data constraints. In addition, the imaged horizontal connections between several anomalies may not be well resolved, and thus should be interpreted with caution.

In the southern region the entire crust is, overall, much less resistive; it ranges from about 300 to 10,000 Ωm. A sharp boundary from a more resistive upper crust to a less resistive lower crust is not observed (mirroring what was observed in the 1-D models). A couple strong (3–30 Ωm), vertically extended anomalies are observed that stretch through the lithosphere (0–80 km; the depth extent beyond this is not well-constrained). It is important to note that these strong anomalies can be identified directly in the data (Figure 8; Figure S2 in Supporting Information S1). The locations appear to be consistent with the proposed locations of important tectonic boundaries in this region (see Section 4.1). To the south, a similar feature exists, although weaker (∼100 Ωm). It is located below a proposed tectonic boundary and appears to be below the projected location of a large mineral zone (Kharmagtai copper and gold deposit, ∼50 km east of the profile).

3.2. Seismic Velocity Models

A temporary seismic array consisting of 69 stations was installed between 102°E–113°E and 42°N–50°N (between the Hangai Dome and the Hentei Mountains) from August 2011 to August 2013, as reported by He et al. (2016) and Zhang et al. (2017). He et al. (2016) used these measurements to carry out a receiver function analysis. Receiver functions are used to detect interfaces, such as the crust–mantle boundary, directly below a measurement by analyzing the converted phases (e.g., P-wave to S-wave conversions). Along, or close to, the MT profile discussed in this study, He et al. (2016) determined that the crust–mantle boundary was at a depth of 43–45 km. Zhao et al. (2021) estimated a slightly greater depth, ∼50 km, for central Mongolia. He et al. (2016)
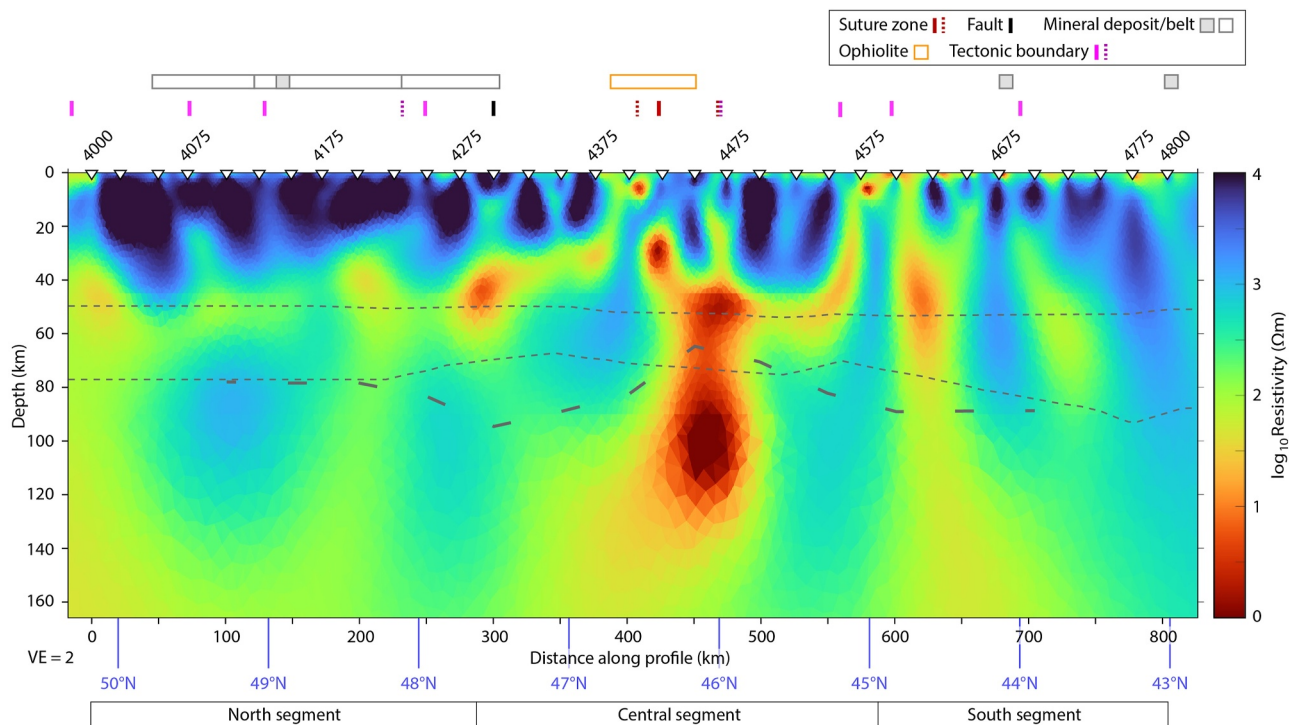
Figure 10. Electrical resistivity model along the profile. The model was generated with the MARE2DEM inversion algorithm (Key, 2016). The locations of 34 MT measurement sites are indicated with triangles at the top of the section. Distances are along the projected profile, which is approximately along longitude 105.5°E (see Figure 1). Vertical exaggeration is a factor of 2. The profile is divided into three segments (north, central, and south). The depth of the (seismically inferred) crust–mantle boundary (∼45 km) and lithosphere–asthenosphere boundary (67–94 km) are drawn based on the model LITHO1.0 (Pasyanos et al., 2014) with dotted gray lines. The 200 Ωm isocontour from the regional 3-D model of Rigaud, Comeau, Kuvshinov, et al. (2023) is marked with a dashed gray line and is taken to represent the approximate depth of the electrical lithosphere-asthenosphere boundary. The proposed locations of the Mongol-Okhotsk suture zone are marked with red lines (see Figure 1) and the location of the Adaatsag ophiolite is shown with an orange box (see Figure 1). Proposed tectonic boundaries, including lithotectonic units such as accreted terranes and an interpreted accretionary wedge, are indicated with pink lines (see Figure 1), and the Hustai fault is marked with a black line (see Figure 1). Additionally, the (projected) boundaries of important mineral deposits and belts are marked with gray boxes, including the Eroo, Boroo, and Zaamar gold belts and the Erdenet copper deposit near the northern part of the profile, and the Kharmagtai and Oyu Tolgoi copper and gold deposits near the southern part. Anomalous features in the lithosphere coincide with the surface position of the Mongol-Okhotsk suture zone and the Adaatsag ophiolite, as well as the Hustai fault zone, in addition to other tectonic boundaries.

obtained Vp/Vs ratios of 1.72–1.78, which are quite high, and concluded that the lower crust of central Mongolia has a high density of ∼3,000 kg/m³ (up to 3,150 kg/m³) and a composition of mafic granulite. This is consistent with global models, such as LITHO1.0 (Pasyanos et al., 2014), which estimates densities of ∼2,800 kg/m³ for the upper and middle crust of the study area and ∼3,000 kg/m³ for the lower-most crust. Furthermore, LITHO1.0 (Pasyanos et al., 2014), which is derived from surface-wave dispersion models, indicates that the lithosphere-asthenosphere boundary varies over depths of 67–94 km across the study area.

Using measurements from the temporary seismic array, Zhang et al. (2017) generated 3-D models of the seismic velocity structure for both P-waves and S-waves. They chose P-wave and S-wave arrivals for earthquake events with a magnitude greater than 5.0 and within an epicentral distance of 30–90° and corrected the travel-time residuals with the CRUST1.0 model and with the crustal thickness determined from the local receiver function study of He et al. (2016). The tomography models were interpolated onto a fine grid of 0.1° by 0.1° and 10 km depth. For comparison with the electrical resistivity model, vertical sections of the velocity models along longitude 105.5° that are nearly coincident with the MT profile and resistivity model are presented in Figures 11a and 12a. These are described below and discussed in the following section. In addition, horizontal slices at selected depths in map view across the study area are presented.

Perturbations of 1%–3% are observed for both the S-wave and P-wave velocity models, with complex and heterogeneous structures. One cannot evaluate the model on a pixel-by-pixel basis but rather on a region-by-region basis (e.g., north, central, south), and clear differences are obvious. However, the very fine structure is not very
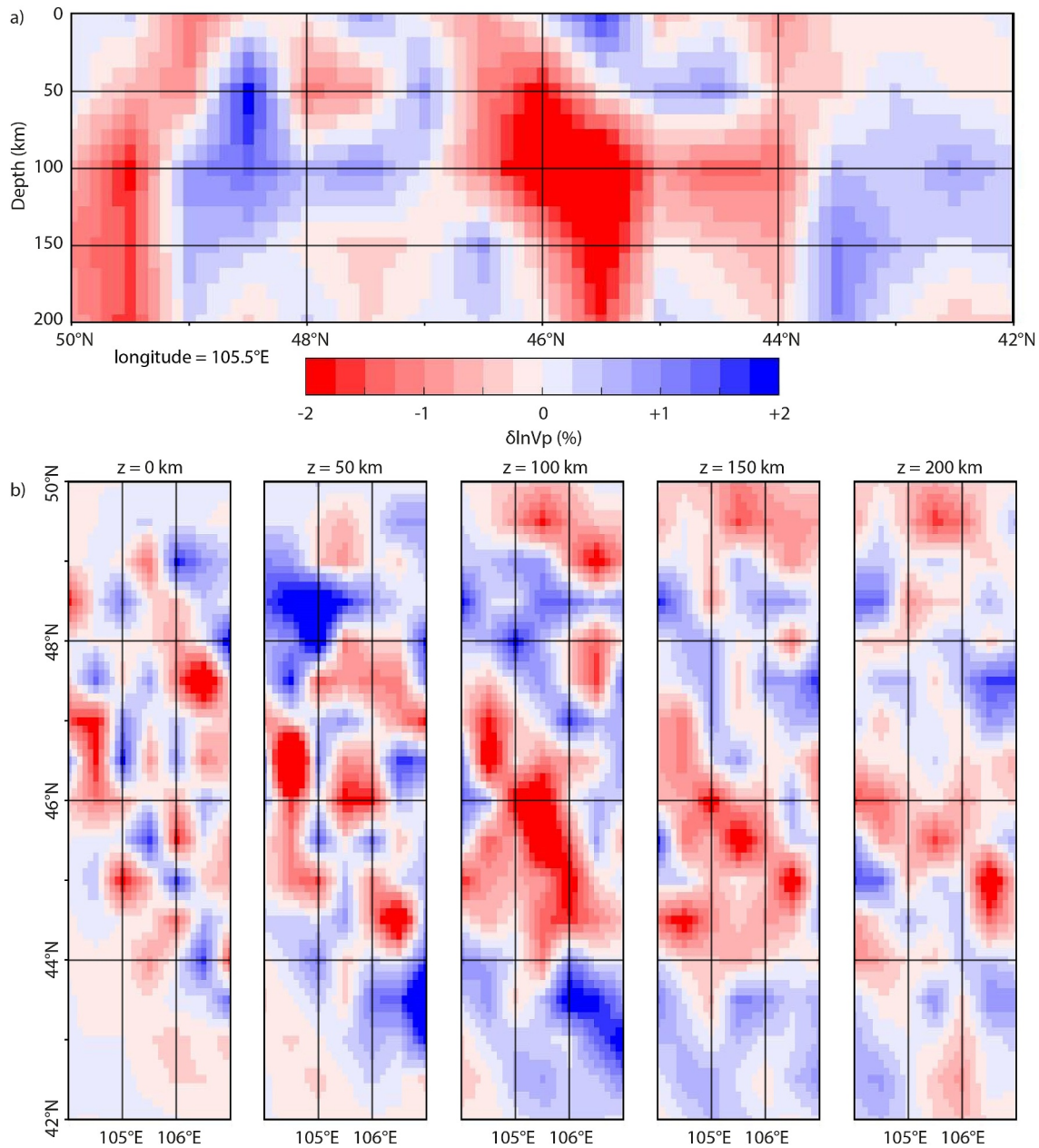
Figure 11. Seismic tomography model showing relative P-wave velocity anomalies. The original model is from Zhang et al. (2017). (a) Vertical sections of the model (latitude against depth) along longitude 105.5°E, nearly coincident with the MT profile. The inferred depth of the crust–mantle boundary is approximately 45–50 km; the lithosphere–asthenosphere boundary varies across the study area, with depths of approximately 70–100 km. The velocity perturbation scale is shown: ±2.0. (b) Horizontal slices in map view (longitude against latitude) for the study area for different depths from 0 to 200 km.

well resolved, particularly in the crust, which may be due in part to the survey design and the underlying physics of the method. Broadly speaking, the central region contains numerous strong anomalies, and, in contrast, the southern region (e.g., south of 45–44°N) has less extreme variations.

The P-wave velocity model shows a strong decrease in the velocity (to −2%) in the central area near 46°N (over 1° wide). In contrast, it shows a general increase in the velocity (1%–2%) north of 47°N and south of 44°N. The anomaly at 46°N appears to be approximately vertically oriented and extends down to greater than 200 km depth. A careful examination of the southern margin of this anomaly shows that it may provide evidence for a southern dipping feature (e.g., from 46.5°N to 45°N, from surface to 100 km depth). Additionally, there are small near-vertical negative anomalies at 49–50°N, 48°N, and 44°N.
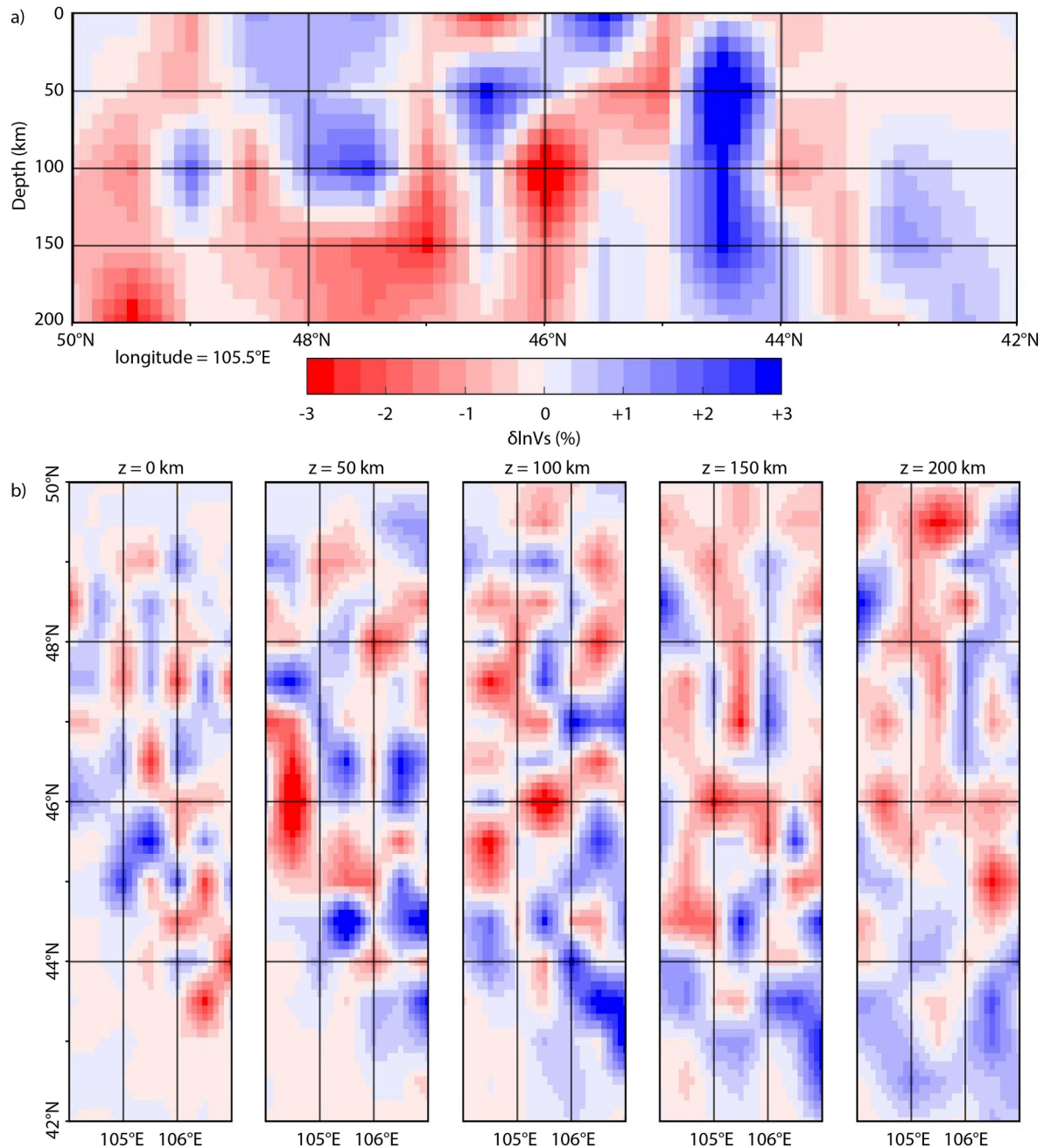
Figure 12. Seismic tomography model showing relative S-wave velocity anomalies. The original model is from Zhang et al. (2017). (a) Vertical sections of the model (latitude against depth) along longitude 105.5°, nearly coincident with the MT profile. The inferred depth of the crust–mantle boundary is approximately 45–50 km; the lithosphere–asthenosphere boundary varies across the study area, with depths of approximately 70–100 km. The velocity perturbation scale is shown: ±3.0%. (b) Horizontal slices in map view (longitude against latitude) for the study area for different depths from 0 to 200 km.

The S-wave velocity model shows a strong decrease in the velocity (to −3%) in the central area near 46°N. This anomaly appears to be vertically oriented and extends from about 50 km depth to greater than 200 km depth. To the south, a strong contrast is observed at 44°N, with a strong increase in the velocity (3%) between 44°N and 45°N that is near-vertical, extending from nearly 0 to 200 km depth. In addition, there are several small positive anomalies (2%–3%), for example, at 46.5°N at 50–100 km depth, 47–48°N near 100 km depth, and at 49°N at 100 km depth, and small near-vertical negative anomalies at 49–50°N, 47°N, and 44°N, from 0 to 200 km depth.

3.2.1. Comparison of Resistivity and Velocity Models

Seismic velocity and electrical resistivity are two independent but complementary physical parameters that can help to distinguish subsurface structures and properties. There is no global relation between resistivity and velocity. Despite this, there is often a spatial correlation between the two parameters (Bedrosian et al., 2004, 2007; Bertrand et al., 2012; Comeau, Becken, & Kuvshinov, 2022; Comeau et al., 2016).

For example, Bedrosian et al. (2007) used a joint interpretation of magnetotelluric and seismic models to infer crustal structure and lithology. One link is through the amount of fluid present (see Bedrosian et al., 2007; Unsworth & Rondenay, 2012): as the amount of fluid increases, resistivity and velocity decrease. The fluid distribution (both aqueous fluids and partial melts) in tectonic zones (subduction or collision), where the circulation of fluids is related to metasomatism, has been investigated with this approach (Unsworth & Rondenay, 2012). However, some variations in rock composition (e.g., chemistry) may influence only one parameter. For example, an increase in the sodium content of a partial melt (e.g., Comeau et al., 2016), miniscule amounts of saline fluids in the crust (e.g., Sheng et al., 2023), or magmatic-hydrothermal fluid flow that causes hydrothermal alteration and sulfide enrichment will strongly decrease the electrical resistivity but will not affect the velocity in a measurable way (Unsworth & Rondenay, 2012).

Comparing multiple geophysical methods, each sensitive to different parameters, can reduce uncertainty when interpreting subsurface models. However, the differences in physics and in resolution between the methods must be considered (e.g., Pritchard et al., 2018; Unsworth et al., 2023). Furthermore, large-scale, regional seismic models may lack the fine resolution possible with a local survey. A joint inversion of both parameters (velocity and resistivity) or a constrained inversion can be advantageous (e.g., Moorkamp et al., 2007), but is not considered in the current study.

A simple qualitative comparison of the resistivity and velocity models from this area reveals some general similarities: the central part has a low-resistivity anomaly and a low-velocity anomaly. This allows us to confidently state that a regional difference exists from north to south across the study area. Furthermore, the locations and patterns of strong S-wave velocity anomalies are strikingly similar to the electrical resistivity model, which, for example, shows high resistivity (>1,000 Ωm) at 44°N vertically oriented, near 47°N at 50–100 km depth, 48°N below 80 km depth, and at 49–50°N below 80 km depth. A comparison of the specific features of the models is continued in the discussion below (Section 4). Different data sets and independent modeling approaches can provide more confidence in the results and interpretation. A properly aligned comparison of the resistivity model and the velocity models is shown in Figure S5 of the Supporting Information S1.

In order to quantitatively compare the resistivity and velocity models in a simple way, a correlation analysis was carried out, following Comeau, Becken, and Kuvshinov (2022). The model sections were divided into a coarse grid, the physical parameters were binned into categories, and the number of occurrences for each combination of parameter categories was counted to look for broad similarities and differences (Figure S6 in Supporting Information S1). Furthermore, zones from the correlation diagram can be mapped to the model space to investigate the spatial correlation. A clear trend, the low-resistivity regions correlate with low P-wave velocity regions and low S-wave velocity regions and the high-resistivity regions correlate with high P-wave velocity regions and high S-wave velocity regions, is observed for the vast majority of cases (85%–90% of the occurrences). A zone of low resistivity and high S-wave velocity was observed, which corresponded spatially to the features between distances of 600–650 km and 400–450 km, as well as 200–300 km. A zone of low P-wave velocity and not low resistivity was observed, and which corresponded to features at distances of 500–600 km. The P-wave velocities and S-wave velocities, which are generally correlated (83% of the occurrences), are not correlated between distances of 600–700 km, and also for some parts between 150 and 400 km. Many reasons could account for the mis-match described above, including small resistivity anomalies that were not observed in the (regional) velocity models, smearing of the models, and resolution differences between techniques, or a physical cause that can reduce the electrical resistivity but not the (S-wave) velocity.

4. Discussion

4.1. Evidence for Lithospheric-Scale Tectonic Boundaries

The Mongol-Okhotsk suture zone is associated with the closure of the Mongol-Okhotsk paleo-ocean. The exact location of many parts of its ∼3,000 km extent are only estimated and are often not agreed upon. However, in the

study area, the exposed Adaatsag ophiolite helps to pinpoint the location of the surface trace. Its subsurface structure and location have, previously, not been well studied. The electrical resistivity models reveal a strong change in the lithospheric structure from the north to the south, and this contrast is indicative of a significant feature related to the history and evolution of the region.

At about 105.5°E and 46–46.5°N, the P-wave and the S-wave velocity models show a strong decrease in the velocity (to −2% and −3%, respectively). The feature is vertically extended and stretches from nearly the surface to depths greater than 200 km. At the same location, the electrical resistivity model shows a low-resistivity zone that is sub-vertical and varies from 1 to 100 Ωm for depths of 0–40 km (mainly the crust), 1–10 Ωm for depths of 40–80 km (mainly in the lower crust and lithospheric mantle), and 1–30 Ωm for depths from 80 km to more than 120 km (mainly in the asthenosphere; the vertical extent is not well resolved), extending slightly to the south. Based on the available information, we interpret this anomaly to represent the Mongol-Okhotsk suture zone, and the results reveal that it is a clear and significant lithospheric-scale boundary. In fact, the geophysical signature likely extends into the upper parts of the asthenosphere.

The region contains various proposed tectonic boundaries that cross the geophysical profiles. For example, at latitudes of ~49.5°N and ~49°N (profile distances of ~75 and ~125 km, respectively), tectonic boundaries, according to Badarch et al. (2002), mark the edges of the Bayangol terrane (described as an island arc) with the Bayangol fault along the southern boundary. Another proposed tectonic boundary at a latitude of 48°N (profile distance of ~250 km) marks the southern edge of the Haraa terrane (described as a backarc/forearc basin) and the location of the Yeroogol fault. As shown in Figure 1, these are large faults that extend for hundreds of kilometers north-east into the Transbaikal region. Furthermore, these areas are important because there are significant mineral zones here. The resistivity model shows narrow low-resistivity anomalies (30–1,000 Ωm) that appear directly below the proposed boundaries of the tectonic domains (at ~49.5°N, ~49°N, and 48°N; profile distances of ~75, ~125, and ~250 km). Although these anomalies are not very conductive, they have a contrast to the highly resistive background (10,000 Ωm). From 49 to 50°N, the P-wave and S-wave models show a velocity reduction (to −1% and −2%). We can conclude that the proposed locations of these tectonic boundaries are sound.

Near 47.5°N (distance ~300 km) a low-resistivity anomaly (1–100 Ωm) stretches through the crust, with a strong signature in the lower crust (depths of ~30–40 km). This feature can also be clearly identified in the data (Figure 8; Figure S2 in Supporting Information S1). The anomaly is located directly below the location of the Hustai fault zone. This provides remarkable insights into the structure of this zone and reveals it is a major crustal feature. The Hustai fault, near the capital city of Ulaanbaatar, is thought to be capable of producing earthquakes larger than magnitude 7 (Ferry et al., 2010), and is thus an important area for research into seismogenic hazards. The electrical resistivity model shows an interesting Y-shaped anomaly (located at a profile distance of ~300 km; size on the order of 10 km), possibly because the fault trace at this specific location is sinuous and passes both north and south of the MT measurement site location 4300 (see Figure 1), thus giving two signatures along the fault. At this location the seismic velocity models show an interesting gradient from low to high of ~2%.

Two tectonic boundaries are proposed near 45°N (profile distance of ~550–600 km). According to Badarch et al. (2002), these are the edges of the Idermeg terrane, described as a passive continental margin, with the Middle Gobi plutonic-volcanic belt to the north (and the Gobi-Altai and Mandalovoo terranes to the south, described as a backarc/forearc basin and an island arc). The resistivity model shows two strong, vertically extended low-resistivity (3–30 Ωm) anomalies that extend over depths of 0–80 km (through the entire lithosphere; the vertical extent beyond this is not well resolved). Between them the crust is ~1,000 Ωm, to the north the crust is ~10,000 Ωm, and to the south the upper crust is ~10,000 Ωm. These anomalies are clearly observed in the data (Figure 8; Figure S2 in Supporting Information S1). The observed locations of the two low-resistivity anomalies are consistent with the proposed locations of the terrane edges. In fact, these are some of the strongest signatures in the model and indicate that these are significant lithospheric-scale boundaries. Near 45°N, the S-wave model shows a small velocity reduction (to −1%) from a depth of 0–100 km, and immediately south a sharp contrast to a strong positive anomaly (+2%) is observed. This may represent the southern edge of this lithotectonic block, and it appears to be a significant boundary.

Another tectonic boundary is proposed near 44°N (profile distance of ~700 km). According to Badarch et al. (2002), the Gurvansayhan terrane lies to the south, described as an island arc (and the Mandalovoo and Gobi-Altai terrane to the north). This is an important area because significant mineral zones are located near the edges of this domain, including the Kharmagtai deposit and Shuteen district near the northern boundary and the Oyu

Tolgoi and Tsagaan Survaga deposits near the southern boundary. Below the proposed location of the tectonic boundary, the resistivity model shows a strong, vertically extended low-resistivity (10–100 Ωm) anomaly that stretches from a depth of 0–80 km (through the entire lithosphere). At 44°N, the P-wave model shows a small velocity reduction (to −1%) from a depth of 0–200 km. Similarly, the S-wave model shows a velocity reduction (to −1%) at 44°N from a depth of 0–200 km, but to the north between 44–45°N there is a strong velocity increase (up to +3%). This contrast in geophysical properties gives evidence for a distinct lithotectonic unit.

We consider the above-discussed anomalies to represent tectonic boundaries. Confirming the location (and number) of tectonic boundaries, as well as their contrasting geophysical properties, can help to understand the history and development of the CAOB. The geophysical signatures likely indicate significantly different rheology and chemical properties than the surroundings (indicative of the independent formation histories of the distinct terranes). The tectonic boundaries and suture zone are likely weak zones, due to pervasive deformation throughout their history, and, furthermore, the boundaries are often associated with mineralization, caused by past fluid flow (e.g., Wannamaker et al., 2002). For the above reasons, the electrical resistivity is reduced in these locations. In addition, there are possible contributions from (sheared) graphite (e.g., Heinson et al., 2005). In particular, compared to the other tectonic boundaries in this study, the imaged lithospheric structure of the Mongol-Okhotsk suture zone appears to be quite broad.

Rather than only a boundary, that is, the suture zone marked by ophiolite at the surface, an alternative explanation is that this feature gives evidence for a downgoing oceanic plate in the lithosphere (cf. Xu et al., 2020). The geophysical anomalies identified at this location, low P-wave velocity, low S-wave velocity, and low resistivity, are observed near the surface at the location of the ophiolite and at depth (∼100 km below and ∼100 km south), and are thus consistent with a southward dipping subduction, as proposed by Sheldrick et al. (2020), or possibly doubly vergent subduction. In this scenario, interconnected conductive minerals, such as magnetite, that are commonly found in serpentinite and in mafic and ultramafic rocks, and which are greatly enhanced by deformation, can explain both the low electrical resistivity and the strong decrease in seismic velocity (Heinson et al., 2005; Robertson et al., 2015, and references therein; Lebedev et al., 2021). Supporting this, Zhu et al. (2023) determined extensive serpentinization (including dunites and harzburgites) around the Adaatsag ophiolite.

4.2. Link Between Deep Features and Mineral Deposit Locations

In the framework of a mineral system approach, a combination of components is required to develop a mineral system, including the presence of sources of metals and fluids and a favorable architecture with fluid-flow pathways (see Huston et al., 2016). To help understand the evolution of a mineral system and the locations of mineral deposit emplacement, both of which help to advance new exploration strategies for the future, knowledge of the whole-lithosphere structure is important.

Ore-forming fluids may be generated from a lithospheric mantle that has been fertilized and metasomatized, possibly by fluids and melts derived from subduction (e.g., Groves et al., 2020, and references therein). Some studies suggest that initial enrichment of metals is an important step (related to fertility; e.g., Zheng et al., 2019). In such a scenario, earlier subduction events or long-lived magmatism may have left (sulfide-bearing) metal-enriched cumulates near the base of the crust that were later re-melted and which provide metal-rich fluids for mineral deposit formation (Holwell et al., 2022; Xu et al., 2021, and references therein). Recent work has drawn links between the surface locations of mineral deposits and narrow conductive features extending through the crust that are attributed to the transport of fluid (e.g., Comeau, Becken, & Kuvshinov, 2022; Heinson et al., 2006, 2018; Sheng et al., 2022), as well as to large conductive features in the deep lithosphere attributed to the sources of ore-forming fluids (e.g., Comeau, Becken, & Kuvshinov, 2022), therefore giving a translithospheric picture of the system. Areas of intense metasomatism will typically have reduced electrical resistivity and reduced seismic velocity (e.g., Jessell et al., 2016).

In the northern part of the study area, several narrow low-resistivity anomalies (30–300 Ωm) are observed in the middle and upper crust. Alone these would be unspectacular, but the contrast to the highly resistive background (10,000 Ωm) is remarkable. A detailed follow-up study with dense measurements could elucidate more of the fine structures and ensure that they are well constrained. Although some of the model features are quite subtle, it is notable that they can be identified directly in the data (Figure 8; Figure S2 in Supporting Information S1). The first (northern-most) anomaly is below the projected location of the Eroo gold belt (see Figures 1 and 10), the second anomaly is below the Boroo gold belt and it is also below the projected location (∼100 km west of profile) of the

Erdenet copper-molybdenum mine, and the third anomaly (which may extend into the lithospheric mantle) is below the projected location of the Zaamar gold belt. In the southern part of the study area a similar type of anomaly, which extends into the lithospheric mantle, is below the projected location (<50 km east of profile) of the Kharmagtai copper-gold mine. The fact that these anomalies appear to be spatially related to the surface locations of large mineral zones and with the locations of proposed tectonic boundaries (see Section 4.1 above) gives information for their interpretation.

One explanation for these small, vertical low-resistivity features is that they may represent the signatures of fossil fluid pathways (possibly from hydrothermal alteration) and record the location of the ascent of ore-forming fluids beneath the metal belt, likely along crustal weaknesses such as tectonic boundaries and faults (e.g., Comeau, Becken, & Kuvshinov, 2022; Heinson et al., 2018; Robertson et al., 2015; Wannamaker et al., 2002). In the lower lithosphere, the low-resistivity features may represent the source region of the ore-forming fluids. Sulfide phases may play a role in causing the low resistivity, for example, if metal-rich (Cu–Au) sulfide melt exists in cumulates near the base of the crust (see Comeau, Becken, & Kuvshinov, 2022, and references therein).

4.3. Are There Hydraulically Connected Lower-Crustal Channels?

MT measurements across the north-central Hangai, 250–400 km to the west, revealed a series of well-resolved, low-resistivity (3–30 Ωm) zones in the lower crust (depth of 30–50 km) beneath a highly resistive upper crust (Comeau, Becken, Connolly, et al., 2020). These are organized into cylinders or tubes with a separation of approximately 25 km, a width of 25 km, and an (east-west) extension of hundreds of kilometers (Käufl, Grayver, Comeau, et al., 2020), which is aligned with GPS measurements that show potential eastward motion of that part of the Hangai block (Calais et al., 2003).

One explanation for these features, proposed by Comeau, Becken, Connolly, et al. (2020) and based on a conceptual model of fluid localization and stagnation by thermally activated compaction (Connolly & Podladchikov, 2004), is consistent with the location, shape, and size of the zones. This explanation hypothesizes that the thermally perturbed lower crust underwent metamorphic dehydration and devolatilization reactions that produced fluids that were subsequently localized in elevated-porosity, fluid-rich domains, and are trapped below the brittle-ductile transition due to an inverted stress gradient. The pattern of fluid focusing is naturally superimposed on large-scale tectonic deformation patterns (e.g., northward continental compression, eastward extrusion). Therefore, it is expected that in three-dimensions these fluid zones form extended channels.

One question that we hoped to answer with the present work was: Do the tube-like lower crustal conductors observed beneath the Hangai extend far to the east? However, the results are ambiguous. The northern segment (northern-most 200 km) of the 2-D model, and the 1-D model, do show a highly resistive upper crust and a low (er)-resistivity lower crust; but the models do not display extreme conductive features (e.g., <10 Ωm). In the southern segment of the profile such a pattern is not observed. It is notable that this is observed to the north of the suture zone but not to the south, further illustrating the distinct regional tectonic domains. Furthermore, the 2-D model might show a pattern of regularly spaced conductive features, but the 25 km measurement spacing in this model, compared to 3–10 km for the Hangai study (Comeau, Becken, Connolly, et al., 2020), is not ideal to determine this conclusively. In addition, a 3-D model from a larger array of data is necessary to image the extension off-profile of any conductive features. Therefore, the model presented here is not inconsistent with the lower crustal conductor observed beneath the Hangai, but the existence of a distinct tube-like pattern is not conclusive.

4.4. Is There Evidence for Mantle Upwellings or Plumes?

What causes the extended, sub-vertical low-velocity structures? Zhang et al. (2017) hypothesized that these features, which extend to depths of more than 300–500 km, represent plumes from the deep upper mantle, or alternatively multiple upwellings of warm mantle, and that they may be responsible for the uplift and magmatism observed in Mongolia. Furthermore, they speculated that the features may be related to deep subduction of the Pacific and Indian plates, located far from Mongolia, with the descending edges of flat stagnant slabs responsible for return flow.

Below central Mongolia, uplift (and magmatism) consistent with that observed was numerically modeled based on an asthenospheric upwelling from a scenario of delamination (due to a thickened and eclogitized crust and a

weak lower crust) or edge-driven convection (related to the substantial step and boundary from a thick lithosphere below the Siberian craton to a thin lithosphere below Mongolia) (Comeau et al., 2021; Stein et al., 2022).

The global model LITHO1.0 (Pasyanos et al., 2014) shows that the thickness of the lithosphere in this region (along longitude 105°E) varies from a maximum of ∼94 km at the edges to a minimum of ∼67 km in the center (between 45.2°N and 47.1°N, or about 350 and 550 km along the resistivity model section). The region with thinner lithosphere is located in the range where low-velocity structures are observed. The Siberian craton boundary is at approximately 52°N, 200 km north of the end of the profile. The thickness of the lithosphere beneath the Siberian craton reaches more than 250 km.

Is the electrical resistivity model consistent with a mantle upwelling? A strong, low-resistivity (<30 Ωm) feature is observed in the electrical resistivity model at 46°N that extends from a depth of about 40 km to more than 120 km, within a background of >300 Ωm. Clearly there is a lateral change in the mantle at this location. The S-wave velocity model shows a strong anomaly (−3%) spatially congruent with the low-resistivity feature. This feature may represent an asthenospheric upwelling. The 2-D electrical resistivity model does not show a deep, continuous layer with a decrease in resistivity that could be attributed to the lithosphere-asthenosphere boundary, in comparison to other models in the region (e.g., Comeau et al., 2018; Käufl, Grayver, Comeau, et al., 2020). However, we note that an increase in the phase for long periods of more than 1,000 s at most sites in the central region is indicative of the increase in conductivity associated with the asthenosphere (see Figure 2).

A recent preliminary regional 3-D model of central Mongolia presented by Rigaud, Comeau, Kuvshinov, et al. (2023) and Rigaud et al. (2024) uses data from a newly acquired array (approximately 400 km by 700 km with ∼50 km spacing; including a subset of the data analyzed here) and thus offers the advantages of a larger aperture and more long-period data, but provides lower resolution. It shows a clear decrease in resistivity between 50–100 km that can be interpreted as the lithosphere-asthenosphere boundary. Specifically, the 200 Ωm contour can be taken to indicate the lithosphere-asthenosphere boundary at a depth of 60–70 km in the center of the profile at 46°N and at a depth of 80–100 km at the edges (see Figure 10) (i.e., a possible a doming shape). In fact, Käufl, Grayver, Comeau, et al. (2020) posited that an upwelling existed beneath the Hangai Dome and that a second upwelling existed east of the Hangai Dome, at the edge of their modeling domain which included all available data at that time.

Given the above, we conclude that the presented model is not inconsistent with the above hypotheses of a mantle upwelling based on the velocity model and geodynamic modeling. In summary, we do not argue for mantle plumes but note that an asthenospheric upwelling, much like the local one proposed below the central Hangai Dome, can be directly reconciled with geodynamic models for delamination or slab break off that can explain the magmatism and mineralization of the region (Comeau et al., 2021; Stein et al., 2022; Tomurtogoo et al., 2005).

An alternative explanation is offered by examining other intriguing regions of the CAOB. Far to the west, near the Junggar Basin (approximately 80°E, 45°N; within the CAOB), Xu et al. (2020) examined evidence for a fossil oceanic plate trapped and preserved in the lithospheric mantle. Whether the anomalies detected below the Mongol-Okhotsk suture zone should be attributed to a broader slab, rather than to a narrow boundary or an altered region, cannot now be answered, but a viable preservation mechanism is required for the former.

The resistivity anomaly observed in the mantle beneath the Mongol-Okhotsk suture zone at 105.5°E and 46°N is very strong. Can partial melt in an upwelling alone explain the conductivity anomaly? Following the parameter estimates and calculations of Comeau, Becken, Grayver, et al. (2022), the strong anomaly (1–10 Ωm) at a depth of 60–80 km (in the lithospheric mantle) could be explained by a minimum of 10% partial melt. However, relations between the relative change in the S-wave velocity and the volume fraction of a minor phase in a two phase system (Chu et al., 2010; Comeau, Becken, Grayver, et al., 2022) indicate that a reduction of 3% in the S-wave velocity implies a partial melt fraction of ∼2.5%. Therefore, this interpretation does not adequately satisfy both geophysical anomalies. However, the addition of a minuscule amount of saline fluids can reduce the amount of partial melt required (e.g., Sheng et al., 2023; Unsworth & Rondenay, 2012).

There are several candidates for mantle minerals that can reduce the velocity and the electrical resistivity. Following Comeau, Becken, Grayver, et al. (2022), we suggest that metasomatism of the lithospheric mantle by subduction is the main cause of both geophysical anomalies. In the lithospheric mantle, the reduction in S-wave velocity can be explained by a more fertile composition (including iron enrichment) (see Begg et al., 2009), and the low electrical resistivity can be explained by the presence of (F-rich) phlogopite and metallic sulfides (both

even in small quantities, e.g., ~0.1%) (see Li et al., 2016), possibly in addition to a network of garnet pyroxenites (e.g., Ferrand & Chin, 2023). Correspondingly (F-rich) phlogopite is compatible with a low S-wave velocity and a fertile mantle enriched in iron is compatible with a low electrical resistivity. Supporting the above explanations, geochemical data analyzed by Sheldrick et al. (2020) indicate metasomatism of a hydrated lithospheric mantle near the Mongol-Okhotsk suture zone and Hunt et al. (2012) determined that the lithospheric mantle below central Mongolia contains phlogopite.

5. Summary and Conclusions

In this study we analyzed MT measurements along a profile (~810 km long) that crosses the Mongol-Okhotsk suture zone and the Adaatsag ophiolite within the CAOB and central Mongolia. Using the SSQ impedances, we examined the apparent resistivity and phase curves for three profile segments (the region north of the suture zone, across the suture zone, and south of the suture zone), and we examined 1-D models of each segment. This showed that the character of the electrical resistivity distribution with depth is distinct in the southern segment. In comparison to the northern segment, where a sharp transition from a highly resistive (up to 10,000 Ωm) upper crust (0–25 km) to a moderately conductive (300–1,000 Ωm) lower crust (25–45 km) is observed, the southern segment has a moderately resistive (800–1,000 Ωm) signature across the entire crust. In the northern segment, the 2-D model shows a few isolated regions of lower resistivity (30–100 Ωm). Broadly speaking, similar lower crustal conductors were observed beneath the Hangai Dome (300–400 km to the west), but with very low resistivities and a distinct tube-like pattern not seen here, that were taken as evidence for hydraulically connected lower-crustal fluid channels oriented fault-parallel in the direction of crustal motion.

Different inversion strategies were tested to generate a 2-D electrical resistivity model and the preferred strategy used a three stage scheme: the algorithm converges in the first stage, enters the Occam smoothing phase in the second stage, and static shifts are computed in the third stage with a reduced error floor. Comparisons of the data and the model response indicated that the model fits the data. We compared the electrical resistivity distribution beneath this region with congruent seismic velocity models for S-waves and P-waves from Zhang et al. (2017). At the location of the Adaatsag ophiolite and the proposed Mongol-Okhotsk suture zone, an anomalous low-resistivity zone (1–100 Ωm) is imaged in the crust and lithospheric mantle. Thus the model reveals a clear and significant lithospheric-scale feature associated with the location of the closure of the Mongol-Okhotsk ocean. The P-wave and S-wave velocity models show a strong decrease in the velocity (to −2% and −3%, respectively) in this same location, with a vertically extended feature stretching from 0 km to greater than 200 km depth. One explanation, satisfying the low resistivity, the significant decrease in seismic velocity, and the ophiolite at the surface, is that this feature may be the signature of a downgoing oceanic plate in the lithosphere, due to extensive serpentinization, and thus may be consistent with hypothesized southward dipping subduction or doubly vergent subduction associated with the closure of the Mongol-Okhotsk ocean.

Across the profile, numerous vertical, narrow, low-resistivity anomalies (1–100 Ωm), which are in contrast to the high resistivity background, are spatially associated with the proposed boundaries of tectonic domains. Confirming the location of tectonic boundaries and geological domains provides insights that help to confirm ideas about the development of the CAOB, which is not fully understood. For example, in the north, the edges of the Haraa terrane, which is bounded by the Bayangol and Yeroogol faults, have prominent signatures. In the south, the edges of the Idermeg terrane have very strong, conductive signatures, possibly of lithospheric-scale. Of particular importance, one such feature (1–100 Ωm) stretches through the crust directly below the location of the Hustai fault zone, marking it as a major crustal feature. This is significant because the Hustai fault, near the capital city of Ulaanbaatar, is thought to be capable of producing large magnitude earthquakes and considerable seismogenic hazards.

The surface locations of large mineral zones hosted in volcanic-plutonic belts that flank the suture zone, specifically the Eroo, Boroo, and Zaamar gold belts, the Erdenet copper-molybdenum mine, and the Kharmagtai copper-gold mine, correspond remarkably well with the vertical crustal electrical resistivity anomalies. These may represent the signatures of fossil fluid pathways. This highlights that the ascent of the ore-forming fluids beneath the metal belts is likely controlled by crustal weaknesses such as the tectonic boundaries and faults.

A doming or upwelling of the asthenosphere is presumed (with up to 30 km difference in height) near the suture zone. This is much like the local one proposed below the central Hangai Dome. Such an asthenospheric upwelling

is consistent with the observed magmatism and uplift as well as with geodynamic models for slab break-off and/or delamination (due to thick and weak lower crust).

Data Availability Statement

The 2-D electrical resistivity input data files and output model response files are available in Rigaud and Comeau (2024) with the repository link as follows: https://doi.org/10.5281/zenodo.10682522. The 2-D electrical resistivity model was generated with the freely available inversion code MARE2DEM (Key, 2016); more details can be found at https://mare2dem.bitbucket.io. The MT data for the Hangai project (2106 and 2017) are available in Käufl, Grayver, Kuvshinov, et al. (2020), with descriptions in Becken et al. (2021a, 2021b).

References

Badarch, G., Cunningham, W. D., & Windley, B. F. (2002). A new subdivision for Mongolia: Implications for the Phanerozoic crustal growth of Central Asia. *Journal of Asian Earth Sciences*, *21*(1), 87–110. https://doi.org/10.1016/S1367-9120(02)00017-2

Becken, M., Kuvshinov, A. V., Comeau, M. J., & Käufl, J. (2021a). Magnetotelluric study of the Hangai Dome, Mongolia. [Data report]. *GFZ Data Services*. https://doi.org/10.5880/GIPP-MT.201613.1

Becken, M., Kuvshinov, A. V., Comeau, M. J., & Käufl, J. (2021b). Magnetotelluric study of the Hangai Dome, Mongolia: Phase II. [Data report]. *GFZ Data Services*. https://doi.org/10.5880/GIPP-MT.201706.1

Becken, M., Ritter, O., & Burkhardt, H. (2008). Mode separation of magnetotelluric responses in three-dimensional environments. *Geophysical Journal International*, *172*(1), 67–86. https://doi.org/10.1111/j.1365-246X.2007.03612.x

Becken, M., Schmalzl, J., Bömer, B., & Ueding, S. (2014). Development of a E-field data logger and of time series processing tools in matlab. In *Proceedings of the 22nd EM induction workshop*. Weimar.

Bedrosian, P. A., Maercklin, N., Weckmann, U., Bartov, Y., Ryberg, T., & Ritter, O. (2007). Lithology-derived structure classification from the joint interpretation of magnetotelluric and seismic models. *Geophysical Journal International*, *170*(2), 737–748. https://doi.org/10.1111/j.1365-246X.2007.03440.x

Bedrosian, P. A., Unsworth, M. J., Egbert, G. D., & Thurber, C. H. (2004). Geophysical images of the creeping segment of the San Andreas Fault: Implications for the role of crustal fluids in the earthquake process. *Tectonophysics*, *385*(1–4), 137–158. https://doi.org/10.1016/j.tecto.2004.02.010

Begg, G. C., Griffin, W. L., Natapov, L. M., O'Reilly, S. Y., Grand, S. P., O'Neill, C. J., et al. (2009). The lithospheric architecture of Africa: Seismic tomography, mantle petrology, and tectonic evolution. *Geosphere*, *5*(1), 23–50. https://doi.org/10.1130/GES00179.1

Bertrand, E. A., Caldwell, T. G., Hill, G. J., Wallin, E. L., Bennie, S. L., Cozens, N., et al. (2012). Magnetotelluric imaging of upper-crustal convection plumes beneath the Taupo Volcanic Zone, New Zealand. *Geophysical Research Letters*, *39*(2), L02304. https://doi.org/10.1029/2011GL050177

Bibby, H. M., Caldwell, T. G., & Brown, C. (2005). Determinable and non-determinable parameters of galvanic distortion in magnetotellurics. *Geophysical Journal International*, *163*(3), 915–930. https://doi.org/10.1111/j.1365-246X.2005.02779.x

Booker, J. (2014). The magnetotelluric phase tensor: A critical review. *Surveys in Geophysics*, *35*(1), 7–40. https://doi.org/10.1007/s10712-013-9234-2

Buchan, C., Cunningham, D., Windley, B. F., & Tomurhuu, D. (2001). Structural and lithological characteristics of the Bayankhongor ophiolite zone, Central Mongolia. *Journal of the Geological Society*, *158*(3), 445–460. https://doi.org/10.1144/jgs.158.3.445

Cagniard, L. (1953). Basic theory of the magnetotelluric method of geophysical prospecting. *Geophysics*, *18*(3), 605–635. https://doi.org/10.1190/1.1437915

Calais, E., Vernolle, M., San'kov, V., Lukhnev, A., Miroshnitchenko, A., Amarjargal, S., & Déverchère, J. (2003). GPS measurements of crustal deformation in the Baikal–Mongolia area (1994–2002): Implications for current kinematics of Asia. *Journal of Geophysical Research*, *108*(B10), 1–14. https://doi.org/10.1029/2002JB002373

Caldwell, T. G., Bibby, H. M., & Brown, C. (2004). The magnetotelluric phase tensor. *Geophysical Journal International*, *158*(2), 457–469. https://doi.org/10.1111/j.1365-246X.2004.02281.x

Chu, R., Helmberger, D. V., Sun, D., Jackson, J. M., & Zhu, L. (2010). Mushy magma beneath Yellowstone. *Geophysical Research Letters*, *37*(1), L01306. https://doi.org/10.1029/2009GL041656

Comeau, M. J., Becken, M., Connolly, J. A. D., Grayver, A., & Kuvshinov, A. V. (2020). Compaction-driven fluid localization as an explanation for lower crustal electrical conductors in an intracontinental setting. *Geophysical Research Letters*, *47*(19), e2020GL088455. https://doi.org/10.1029/2020GL088455

Comeau, M. J., Becken, M., Grayver, A. V., Käufl, J., & Kuvshinov, A. (2022). The geophysical signature of a continental intraplate volcanic system: From surface to mantle source. *Earth and Planetary Science Letters*, *587*, 117307. https://doi.org/10.1016/j.epsl.2021.117307

Comeau, M. J., Becken, M., Käufl, J. S., Grayver, A. V., Kuvshinov, A. V., Tserendug, S., et al. (2020). Evidence for terrane boundaries and suture zones across southern Mongolia detected with a 2-dimensional magnetotelluric transect. *Earth Planets and Space*, *72*(5), 1–13. https://doi.org/10.1186/s40623-020-1131-6

Comeau, M. J., Becken, M., & Kuvshinov, A. (2022). Imaging the whole-lithosphere structure of a mineral system—Geophysical signatures of the sources and pathways of ore-forming fluids. *Geochemistry, Geophysics, Geosystems*, *23*(8), e2022GC010379. https://doi.org/10.1029/2022GC010379

Comeau, M. J., Käufl, J. S., Becken, M., Kuvshinov, A. V., Grayver, A. V., Kamm, J., et al. (2018). Evidence for fluid and melt generation in response to an asthenospheric upwelling beneath the Hangai Dome, Mongolia. *Earth and Planetary Science Letters*, *487*, 201–209. https://doi.org/10.1016/j.epsl.2018.02.007

Comeau, M. J., Stein, C., Becken, M., & Hansen, U. (2021). Geodynamic modeling of lithospheric removal and surface deformation: Application to intraplate uplift in central Mongolia. *Journal of Geophysical Research: Solid Earth*, *126*(5), e2020JB021304. https://doi.org/10.1029/2020JB021304

Comeau, M. J., Unsworth, M. J., & Cordell, D. (2016). New constraints on the magma distribution and composition beneath Volcán Uturuncu and the southern Bolivian Altiplano from magnetotelluric data. *Geosphere*, *12*(5), 1391–1421. https://doi.org/10.1130/GES01277.1

Connolly, J. A. D., & Podladchikov, Y. Y. (2004). Fluid flow in compressive tectonic settings: Implications for midcrustal seismic reflectors and downward fluid migration. *Journal of Geophysical Research*, *109*, B4. https://doi.org/10.1029/2003JB002822

Dejidmaa, G. (1996). Gold metallogeny of Mongolia. *Mongolian Geoscientist*, *1*, 6–29.

A. B. Dergunov (Ed.) (2001). *Tectonics, magmatism and metallogeny of Mongolia* (p. 304). Taylor & Francis. https://doi.org/10.4324/9780203017975

Dilek, Y., & Furnes, H. (2014). Ophiolites and their origins. *Elements*, *10*(2), 93–100. https://doi.org/10.2113/gselements.10.2.93

Ferrand, T. P., & Chin, E. J. (2023). Garnet pyroxenites explain high electrical conductivity in the East African deep lithosphere. *Lithos*, *462–463*, 107405. https://doi.org/10.1016/j.lithos.2023.107405

Ferry, M., Schlupp, A., Munkhuur, U., Munschy, M., Fleury, S., Baatarsuren, G., et al. (2010). Tectonic morphology of the Hustai Fault (northern Mongolia), A source of seismic hazard for the city of Ulaanbaatar. In *Abstracts for the European geosciences union (EGU) general assembly 2010*. EGU2010-11122. Retrieved from https://meetingorganizer.copernicus.org/EGU2010/EGU2010-11122.pdf

Grayver, A. V., & Kuvshinov, A. V. (2016). Exploring equivalence domain in nonlinear in-verse problems using Covariance Matrix Adaption Evolution Strategy (CMAES) and random sampling. *Geophysical Journal International*, *205*(2), 971–987. https://doi.org/10.1093/gji/ggw063

Groom, R. W., & Bailey, R. C. (1989). Decomposition of magnetotelluric impedance tensors in the presence of local three-dimensional galvanic distortion. *Journal of Geophysical Research*, *94*(B2), 1913–1925. https://doi.org/10.1029/JB094iB02p01913

Groves, D. I., Zhang, L., & Santosh, M. (2020). Subduction, mantle metasomatism, and gold: A dynamic and genetic conjunction. *GSA Bulletin*, *132*(7–8), 1419–1426. https://doi.org/10.1130/B35379.1

Guy, A., Schulmann, K., Munschy, M., Miege, J. M., Edel, J. B., Lexa, O., & Fairhead, D. (2014). Geophysical constraints for terrane boundaries in southern Mongolia. *Journal of Geophysical Research: Solid Earth*, *119*(10), 7966–7991. https://doi.org/10.1002/2014JB011026

He, J., Wu, Q., Sandvol, E., Ni, J., Gallegos, A., Gao, M., et al. (2016). The crustal structure of south central Mongolia using receiver functions. *Tectonics*, *35*(6), 1392–1403. https://doi.org/10.1002/2015TC004027

Heinson, G., Didana, Y., Soeffky, P., Thiel, S., & Wise, T. (2018). The crustal geophysical signature of a world-class magmatic mineral system. *Scientific Reports*, *8*(1), 10608. https://doi.org/10.1038/s41598-018-29016-2

Heinson, G., White, A., & Lilley, F. E. M. (2005). Rifting of a passive margin and development of a lower-crustal detachment zone: Evidence from marine magnetotellurics. *Geophysical Research Letters*, *32*(12), L12305. https://doi.org/10.1029/2005GL022934

Heinson, G. S., Direen, N. G., & Gill, R. M. (2006). Magnetotelluric evidence for a deep-crustal mineralizing system beneath the Olympic Dam iron oxide copper-gold deposit, southern Australia. *Geology*, *34*(7), 573–576. https://doi.org/10.1130/G22222.1

Holwell, D. A., Fiorentini, M. L., Knott, T. R., McDonald, I., Blanks, D. E., McCuaig, T. C., & Gorczyk, W. (2022). Mobilisation of deep crustal sulfide melts as a first order control on upper lithospheric metallogeny. *Nature Communications*, *13*(1), 573. https://doi.org/10.1038/s41467-022-28275-y

Hunt, A. C., Parkinson, I. J., Harris, N. B. W., Barry, T. L., Rogers, N. W., & Yondon, M. (2012). Cenozoic volcanism on the Hangai Dome, Central Mongolia: Geochemical evidence for changing melt sources and implications for mechanisms of melting. *Journal of Petrology*, *53*(9), 1913–1942. https://doi.org/10.1093/petrology/egs038

Huston, D. L., Mernagh, T. P., Hagemann, S. G., Doublier, M. P., Fiorentini, M., Champion, D. C., et al. (2016). Tectono-metallogenic systems–The place of mineral systems within tectonic evolution, with an emphasis on Australian examples. *Ore Geology Reviews*, *76*, 168–210. https://doi.org/10.1016/j.oregeorev.2015.09.005

Jessell, M. W., Begg, G. C., & Miller, M. S. (2016). The geophysical signatures of the West African Craton. *Precambrian Research*, *274*, 3–24. https://doi.org/10.1016/j.precamres.2015.08.010

Jin, S., Sheng, Y., Comeau, M. J., Becken, M., Wei, W., Ye, G., et al. (2022). Relationship of the crustal structure, rheology, and tectonic dynamics beneath the Lhasa-Gangdese terrane (southern Tibet) based on a 3-D electrical model. *Journal of Geophysical Research: Solid Earth*, *127*(11), e2022JB024318. https://doi.org/10.1029/2022JB024318

Jones, A. G. (2006). Electromagnetic interrogation of the anisotropic Earth: Looking into the Earth with polarized spectacles. *Physics of the Earth and Planetary Interiors*, *158*(2–4), 281–291. https://doi.org/10.1016/j.pepi.2006.03.026

Käufl, J. S., Grayver, A. V., Comeau, M. J., Kuvshinov, A. V., Becken, M., Batmagnai, E., & Demberel, S. (2020). Magnetotelluric multiscale 3-D inversion reveals crustal and upper mantle structure beneath the Hangai and Gobi-Altai region in Mongolia. *Geophysical Journal International*, *221*(2), 1002–1028. https://doi.org/10.1093/gji/ggaa039

Käufl, J. S., Grayver, A. V., Kuvshinov, A., Comeau, M. J., Becken, M., Batmagnai, E., et al. (2020). The Hangai mountains magnetotelluric experiment: Data repository [Dataset]. *ETH Zurich Research Collection*. https://doi.org/10.3929/ethz-b-000412346

Key, K. (2016). MARE2DEM: A 2D inversion code for controlled-source electromagnetic and magnetotelluric data. *Geophysical Journal International*, *207*(1), 571–588. https://doi.org/10.1093/gji/ggw290

Khishgee, C., & Akasaka, M. (2015). Mineralogy of the Boroo gold deposit in the North Khentei gold belt, central northern Mongolia. *Resource Geology*, *65*(4), 311–327. https://doi.org/10.1111/rge.12073

Kovach, V., Salnikova, E., Wang, K., Jahn, B., Chiu, H., Reznitskiy, L., et al. (2013). Zircon ages and Hf isotopic constraints on sources of clastic metasediments of the Slyudyansky high-grade complex, southeastern Siberia: Implication for continental growth and evolution of the Central Asian Orogenic Belt. *Journal of Asian Earth Sciences*, *62*, 18–36. https://doi.org/10.1016/j.jseaes.2011.08.008

Kravchinsky, V. A., Cogne, J. P., Harbert, W. P., & Kuzmin, M. I. (2002). Evolution of the Mongol–Okhotsk Ocean as constrained by new paleomagnetic data from the Mongol–Okhotsk suture zone, Siberia. *Geophysical Journal International*, *148*(1), 34–57. https://doi.org/10.1046/j.1365-246x.2002.01557.x

Kröner, A., Lehmann, J., Schulmann, K., Demoux, A., Lexa, O., Tomurhuu, D., et al. (2010). Lithostratigraphic and geochronological constraints on the evolution of the Central Asian Orogenic Belt in SW Mongolia: Early Paleozoic rifting followed by late Paleozoic accretion. *American Journal of Science*, *310*(7), 523–574. https://doi.org/10.2475/07.2010.01

Lebedev, E. B., Kern, H., Pavlenkova, N. I., Lukanin, O. A., Lobanov, K. V., Zharikov, A. V., & Popp, T. (2021). Compressional wave velocity measurements on mafic–ultramafic rocks under high aqueous fluid pressure and temperature help to explain low-velocity zones in the lithosphere. *Scientific Reports*, *11*(1), 13424. https://doi.org/10.1038/s41598-021-92248-2

Li, Y., Yang, X., Yu, J. H., & Cai, Y. F. (2016). Unusually high electrical conductivity of phlogopite: The possible role of fluorine and geophysical implications. *Contributions to Mineralogy and Petrology*, *171*(4), 37. https://doi.org/10.1007/s00410-016-1252-x

McNeice, G. W., & Jones, A. G. (2001). Multisite, multifrequency tensor decomposition of magnetotelluric data. *Geophysics*, *66*(1), 158–173. https://doi.org/10.1190/1.1444891

Mineral Resources Authority of Mongolia. (2014). Present situation of mineral resources of Mongolia. Retrieved from http://www.mram.gov.mn

Moorkamp, M., Jones, A. G., & Eaton, D. W. (2007). Joint inversion of teleseismic receiver functions and magnetotelluric data using a genetic algorithm: Are seismic velocities and electrical conductivities compatible? *Geophysical Research Letters*, *34*(16), L16311. https://doi.org/10.1029/2007GL030519

Pasyanos, M. E., Masters, T. G., Laske, G., & Ma, Z. (2014). LITHO1.0: An updated crust and lithospheric model of the Earth. *Journal of Geophysical Research: Solid Earth*, *119*(3), 2153–2173. https://doi.org/10.1002/2013JB010626

Pritchard, M. E., de Silva, S., Michelfelder, G., Zandt, G., McNutt, S., Gottsmann, J., et al. (2018). Synthesis: PLUTONS: Investigating the relationship between pluton growth and volcanism in the Central Andes. *Geosphere*, *14*(3), 954–982. https://doi.org/10.1130/GES01578.1

Rigaud, R., & Comeau, M. J. (2024). Electrical resistivity model along a profile crossing the Mongol–Okhotsk suture zone, Adaatsag ophiolite, and tectonic boundaries of the Central Asian Orogenic Belt (Mongolia) [Dataset]. *Zenodo*. https://doi.org/10.5281/zenodo.10682522

Rigaud, R., Comeau, M. J., Becken, M., Kuvshinov, A., Kruglyakov, M., Tserendug, S., et al. (2024). Magnetotelluric data across western, central, and eastern Mongolia: Report on new measurements, new models, and implications for intracontinental deformation, deep mineral systems, and intraplate volcanism. In *Abstracts for the European geosciences union (EGU) general assembly 2024* (pp. EGU24–5602). https://doi.org/10.5194/egusphere-egu24-5602

Rigaud, R., Comeau, M. J., Becken, M., Kuvshinov, A. V., Tserendug, S., Batmagnai, E., & Demberel, S. (2023). Magnetotelluric data across Mongolia: Implications for intracontinental deformation and intraplate volcanism—Report on new measurements. In *Abstracts for the European geosciences union (EGU) general assembly 2023* (pp. EGU23–9485). https://doi.org/10.5194/egusphere-egu23-9485

Rigaud, R., Comeau, M. J., Kuvshinov, A. V., Grayver, A., Batmagnai, E., Tserendug, S., et al. (2023). Extending magnetotelluric study from central to eastern Mongolia: Preliminary 2-D and 3-D inversion results. In *Abstracts for the international union of geodesy and Geophysics (IUGG) general assembly 2023*. IUGG23-4312. https://doi.org/10.57757/IUGG23-4312

Robertson, K., Taylor, D., Thiel, S., & Heinson, G. (2015). Magnetotelluric evidence for serpentinisation in a Cambrian subduction zone beneath the Delamerian Orogen, southeast Australia. *Gondwana Research*, *28*(2), 601–611. https://doi.org/10.1016/j.gr.2014.07.013

Rung-Arunwan, T., Siripunvaraporn, W., & Utada, H. (2016). On the Berdichevsky average. *Physics of the Earth and Planetary Interiors*, *253*, 1–4. https://doi.org/10.1016/j.pepi.2016.01.006

Sheldrick, T., Barry, T., Millar, I., Barfod, D., Halton, A., & Smith, D. (2020). Evidence for southward subduction of the Mongol-Okhotsk oceanic plate: Implications from Mesozoic adakitic lavas from Mongolia. *Gondwana Research*, *79*, 140–156. https://doi.org/10.1016/j.gr.2019.09.007

Sheng, Y., Jin, S., Comeau, M. J., Becken, M., Zhang, L., Dong, H., et al. (2022). Controls on the metallogenesis of the Lhasa–Mozugongka district, Gangdese Belt, Tibetan Plateau: Constraints on melt distribution and viscosity from the 3-D electrical structure of the lithosphere. *Ore Geology Reviews*, *145*, 104881. https://doi.org/10.1016/j.oregeorev.2022.104881

Sheng, Y., Jin, S., Comeau, M. J., Dong, H., Zhang, L., Lei, L., et al. (2021). Lithospheric structure near the northern Xainza-Dinggye rift, Tibetan Plateau–implications for rheology and tectonic dynamics. *Journal of Geophysical Research: Solid Earth*, *126*(8), e2020JB021442. https://doi.org/10.1029/2020JB021442

Sheng, Y., Jin, S., Comeau, M. J., Hou, Z., Becken, M., Dong, H., et al. (2023). Evidence for partial melting and alkali-rich fluids in the crust from a 3-D electrical resistivity model in the vicinity of the Coqen region, western Lhasa terrane, Tibetan Plateau. *Earth and Planetary Science Letters*, *619*, 118316. https://doi.org/10.1016/j.epsl.2023.118316

Sillitoe, R. H., Gerel, O., Dejidma, G., Gotovsuren, A., Sanjaadorj, D., Baasanjdorj, S., & Bat-Erdene, D. (1996). Mongolia's gold potential. *Mining Magazine*, 12–15.

Simpson, F., & Bahr, K. (2005). *Practical magnetotellurics*. Cambridge University Press. https://doi.org/10.1017/CBO9780511614095.003

Singer, D. A., Berger, V. I., & Moring, B. C. (2008). *Porphyry copper deposits of the world: Database and grade and tonnage models*. U.S. Geological Survey Open-File Report 2008-1155. Retrieved from https://pubs.usgs.gov/of/2008/1155/

Stein, C., Comeau, M. J., Becken, M., & Hansen, U. (2022). Numerical study on the style of delamination. *Tectonophysics*, *827*, 229276. https://doi.org/10.1016/j.tecto.2022.229276

Styron, R. (2018). Gem foundation global active faults project (GEM-GAF). https://doi.org/10.5281/zenodo.1404388

Tomurtogoo, O., Windley, B. F., Kroner, A., Badarch, G., & Liu, D. Y. (2005). Zircon age and occurrence of the Adaatsag ophiolite and Muron shear zone, central Mongolia: Constraints on the evolution of the Mongol-Okhotsk Ocean, suture and orogeny. *Journal of the Geological Society. London*, *162*, 197–229. https://doi.org/10.1144/0016-764903-14

Türkoğlu, E., Unsworth, M., Çağlar, İ., Tuncer, V., & Avşar, Ü. (2008). Lithospheric structure of the Arabia-Eurasia collision zone in eastern Anatolia: Magnetotelluric evidence for widespread weakening by fluids? *Geology*, *36*(8), 619–622. https://doi.org/10.1130/G24683A.1

Unsworth, M., Comeau, M. J., Diaz, D., Brasse, H., Heit, B., Favetto, A., et al. (2023). Crustal structure of the Lazufre volcanic complex and the southern Puna from 3-D inversion of magnetotelluric data: Implications for surface uplift and evidence for melt storage and hydrothermal fluids. *Geosphere*, *19*(5), 1210–1230. https://doi.org/10.1130/GES02506.1

Unsworth, M. J., & Rondenay, S. (2012). Mapping the distribution of fluids in the crust and lithospheric mantle utilizing geophysical methods. In D. E. Harlov, & H. Austrheim (Eds.), *Metasomatism and the chemical transformation of rock* (pp. 535–598). Springer. https://doi.org/10.1007/978-3-642-28394-9_13

Van der Voo, R., van Hinsbergen, D. J. J., Domeier, M., Spakman, W., & Torsvik, T. H. (2015). Latest Jurassic–earliest Cretaceous closure of the Mongol-Okhotsk Ocean: A paleomagnetic and seismological-tomographic analysis. *Geological Society of America Special Paper*, *513*, 589–606. https://doi.org/10.1130/2015.2513(19)

Walker, R. T., Nissen, E., Molor, E., & Bayasgalan, A. (2007). Reinterpretation of the active faulting in central Mongolia. *Geology*, *35*(8), 759–762. https://doi.org/10.1130/G23716A.1

Wang, T., Ma, G., Comeau, M. J., Becken, M., Zhou, Z., Liu, W., et al. (2022). Evidence for the superposition of tectonic systems in the northern Songliao Block, NE China, revealed by a 3-D electrical resistivity model. *Journal of Geophysical Research: Solid Earth*, *127*(4), e2021JB022827. https://doi.org/10.1029/2021JB022827

Wannamaker, P. E., Hasterok, D. P., Johnston, J. M., Stodt, J. A., Hall, D. B., Sodergren, T. L., et al. (2008). Lithospheric dismemberment and magmatic processes of the Great Basin–Colorado Plateau transition, Utah, implied from magnetotellurics. *Geochemistry, Geophysics, Geosystems*, *9*(5), Q05019. https://doi.org/10.1029/2007GC001886

Wannamaker, P. E., Jiracek, G. R., Stodt, J. A., Caldwell, T. G., Gonzalez, V. M., McKnight, J. D., & Porter, A. D. (2002). Fluid generation and pathways beneath an active compressional orogen, the New Zealand Southern Alps, inferred from magnetotelluric data. *Journal of Geophysical Research*, *107*(B2), ETG6-1–ETG6-20. https://doi.org/10.1029/2001JB000186

Weidelt, P. (1972). The inverse problem of geomagnetic induction. *Journal of Geophysics*, *38*, 257–289.

Xu, B., Hou, Z. Q., Griffin, W. L., Lu, Y., Belousova, E., Xu, J. F., & O'Reilly, S. Y. (2021). Recycled volatiles determine fertility of porphyry deposits in collisional settings. *American Mineralogist*, *106*(4), 656–661. https://doi.org/10.2138/am-2021-7714

Xu, Y. X., Yang, B., Zhang, A., Wu, S., Zhu, L., Yang, Y., et al. (2020). Magnetotelluric imaging of a fossil oceanic plate in northwestern Xinjiang, China. *Geology*, *48*(4), 385–389. https://doi.org/10.1130/G47053.1

Yin, A. (2010). Cenozoic evolution of Asia: A preliminary synthesis. *Tectonophysics*, *488*(1–4), 293–325. https://doi.org/10.1016/j.tecto.2009.06.002

Zhang, F., Wu, Q., Grand, S., Li, Y., Gao, M., Demberel, S., et al. (2017). Seismic velocity variations beneath central Mongolia: Evidence for upper mantle plumes? *Earth and Planetary Science Letters*, *459*, 406–416. https://doi.org/10.1016/j.epsl.2016.11.053

Zhao, H., Wang, P., & Huang, Z. (2021). Lithospheric structures beneath the western Mongolian Plateau: Insight from S wave receiver function. *Journal of Asian Earth Sciences*, *212*, 104733. https://doi.org/10.1016/j.jseaes.2021.104733

Zhao, P., Xu, B., & Jahn, B. M. (2017). The Mongol-Okhotsk Ocean subduction related Permian peraluminous granites in northeastern Mongolia: Constraints from zircon U-Pb ages, whole-rock elemental and Sr-Nd-Hf isotopic compositions. *Journal of Asian Earth Sciences*, *144*, 225–242. https://doi.org/10.1016/j.jseaes.2017.03.022

Zheng, Y.-C., Liu, S.-A., Wu, C.-D., Griffin, W. L., Li, Z.-Q., Xu, B., et al. (2019). Cu isotopes reveal initial Cu enrichment in sources of giant porphyry deposits in a collisional setting. *Geology*, *47*(2), 135–138. https://doi.org/10.1130/G45362.1

Zhu, M., Pastor-Galán, D., Miao, L., Zhang, F., Ganbat, A., Li, A., et al. (2023). Evidence for early Pennsylvanian subduction initiation in the Mongol–Okhotsk Ocean from the Adaatsag ophiolite (Mongolia). *Lithos*, *436–437*, 106951. https://doi.org/10.1016/j.lithos.2022.106951